

RBG-Maxwell Framework: Simulation of Collisional Plasma Systems via Coupled Boltzmann-Maxwell equations on GPU

Ming-Yan Sun

Xi'an Research Institute of High Tech, Xi'an 710021, China,

Peng Xu

Xi'an Research Institute of High Tech, Xi'an 710021, China.

Jun-Jie Zhang*

*Division of Computational Physics and Intelligent Modeling,
Northwest Institute of Nuclear Technology, Xi'an 710024, China,*

Qun Wang

Department of Modern Physics, University of Science and Technology of China, Hefei 230026, China

Tai-Jiao Du

*Division of Computational Physics and Intelligent Modeling,
Northwest Institute of Nuclear Technology, Xi'an 710024, China.*

Jian-Guo Wang*

*School of Information and Communications Engineering,
Xi'an Jiaotong University, Xi'an 710049, China**

(Dated: August 10, 2023)

This paper presents the RBG-Maxwell framework, a relativistic collisional plasma simulator on GPUs. We provide detailed discussions on the fundamental equations, numerical algorithms, implementation specifics, and key testing outcomes. The RBG-Maxwell framework is a robust numerical code designed for simulating the evolution of plasma systems through a kinetic approach on large-scale GPUs. It offers easy adaptability to a wide range of physical systems. Given the appropriate initial distributions, particle masses, charges, differential cross-sections, and external forces (which are not confined to electromagnetic forces), the RBG-Maxwell framework can direct the evolution of a particle system from a non-equilibrium state to a thermal state.

I. INTRODUCTION

As the fourth state of matter along with the solid, liquid and gas, the plasma comprises 99% of the visible universe, ranging from the quark-gluon matter at microscopic scales to plasma at macroscopic scales [1]. The self-consistent interaction of charged particles with electromagnetic (EM) fields is essential to describe many plasma systems such as the early universe [2], plasma [3, 4], Tokamak [5, 6], high-altitude nuclear explosion [7–9], vacuum electronic devices [10–12], system generated EM pulses [13–15], and solar plasma, etc.

The self-consistent plasma model involves the classical EM fields governed by Maxwell equations and the particle distributions in coordinate space (phase space) governed by conservation (kinetic or Boltzmann) equations. These equations are coupled to each other, namely, the particles are sources to the fields while the fields exert forces on the particles. In some cases, the particles can have radiations (including α , β or γ rays depending on energy scales) in quantum transition processes. These particles and radiations as well as the EM fields all interact with one another both classically and in quantum processes, forming a complex system of particles and fields at a wide range of energy scales. We take a plasma of ionized hydrogen and electrons as an example. The mass of an H^+ ion is about 1836 times that of an electron, but they have the same electric charge. Thus, the two species are at extremely different space-time (or energy) scales under the influence of the same EM fields: electrons can be easily accelerated even to the speed of light while it is much harder for ions. This multi-scale feature is one of the major challenges in a theoretical

*corresponding authors: Jian-Guo Wang E-mail address: wanguiuc@mail.xjtu.edu.cn;
Jun-Jie Zhang E-mail address: zjacob@mail.ustc.edu.cn;
To use our code, please refer to <https://Juenjie.github.io> or <https://sunminmgyan.github.io>

description of plasma system [16].

Due to the multi-scale feature and many physical processes in some plasma systems, most theoretical models are focused on specific phenomena at some particular scales. In general these models can be put into three categories: fluid dynamics models coupled with Maxwell equations [17–19], the kinetic ion models with ions treated as particles and electrons as fluids [20, 21], and the fully kinetic models [22–25]. The general-purpose plasma toolkits also emerged in recent years beyond the fields in which they had originally been developed [26, 27].

There are mainly two numerical methods to solve the coupled Boltzmann equations and Maxwell equations self-consistently: the particle simulation method (e.g., the Particle-In-Cell method [28–33] and the test particle method [24, 34–36], etc.) and the direct numerical method [37–40]. The two approaches have their own pros and cons in some circumstances. For instance, the particle simulation method has an advantage in describing complex moving geometries and high-deformation flows, while the direct numerical method is more suitable for large scale and collisional plasma systems. Since the latter is numerically more challenging than the former, not many studies have been carried out in this direction.

The full numerical solution to the Boltzmann equation (BE) has always been a computational challenge due to its high-dimension collisional integrals even on today’s petascale CPU clusters [41, 42]. With the advent of Graphic Processing Unit (GPU) technology in parallel computing, some calculations become feasible [43–47]. In this paper, we focus on the direct numerical method to solve the Relativistic Boltzmann equations on GPUs coupled with Maxwell equations (the RBG-Maxwell framework) for collisional plasma.

The RBG-Maxwell framework contains following main modules as building blocks.

- A module for calculating the collision terms of the BE. The evaluation of collision terms is made by ZMCintegral, a high-dimension integration package based on GPU [48, 49]. All interactions among particles and radiations are incorporated into collision terms through the matrix elements for particle scatterings in quantum theory [50, 51].

- A module for calculating the drift terms of the BE. The drift term in the left hand side of the BE describes the variation of the particle’s distribution in phase space due to its velocity and the force exerted on it. The latter is also called the Vlasov term which describes the drift of the particle from classical fields such as the EM and gravitational fields.

- A module for calculating the EM fields. We solve Jefimenko’s equations for the EM fields as functions of space and time. The source terms for Jefimenko’s equations are determined from the distribution functions of charged particles, whose evolution is governed by the BE. An open source version of this module, JefiGPU [52], can be found and executed on the Code Ocean platform.

- A module to couple the BE to Maxwell equations. The distribution functions of charged particles at one time play as inputs (the source terms) to JefiGPU to give the EM fields at the same time which play as inputs back to the BE to obtain the distribution functions at the next time step. The loop continues till the end of the evolution at the final time.

The purpose of the RBG-Maxwell framework is to build a general simulation toolkit for collisional plasma. It can be applied to various plasma systems such as pre-equilibrium state of quark-gluon plasma in high energy heavy-ion collisions [53–57], solar plasma in collisions [58, 59], collisional plasma involving quantum states [60–62] or particle annihilation/production/ionization [63], etc..

II. UNIT AND CONVENTIONS

A. Natural unit

Throughout this work, we use the natural unit (NU) with the reduced Planck constant \hbar , the speed of light c , the vacuum permittivity ϵ_0 and the Boltzmann constant k_B as basis units. In different scenarios, we may choose different numerical values for \hbar , c , k_B and ϵ_0 that are appropriate for specific phenomena of interest at different energy scales. The dimension of a physical quantity can be expressed as $\hbar^\alpha c^\beta k_B^\gamma \epsilon_0^\delta$. For example, the proton’s charge e (electron’s charge without sign), which is 1.06×10^{-19} Coulomb in the international unit system (SI), is $e = 0.302862\sqrt{\hbar c \epsilon_0}$ in NU, being obtained from the fine structure constant $\alpha = e^2/(4\pi\epsilon_0\hbar c) \approx 1/137$. Any physical quantity in NU has the dimension of the energy to some power if we set $\hbar = c = k_B = \epsilon_0 = 1$. This is called the NU convention. Normally, the energy unit is MeV in NU or NU convention, for example, the electron mass is 0.511 MeV and one second is 1.5×10^{21} MeV⁻¹, etc..

In order to show how to convert a quantity between NU and SI, we start with the values of \hbar and c in SI,

$$\begin{aligned} \hbar &= 1.05457 \times 10^{-34} \text{J}\cdot\text{s}, \\ c &= 2.99792 \times 10^8 \text{m/s}. \end{aligned} \tag{1}$$

Table I: Conversion between SI and NU.

quantity	SI	NU
length	m	$3.16304 \times 10^{25} \hbar c \lambda \text{ E}^{-1}$
mass	kg	$8.89752 \times 10^{16} / (\lambda c^2) \text{ E}$
time	s	$9.48253 \times 10^{33} \hbar \lambda \text{ E}^{-1}$
momentum	kg·m/s	$2.99792 \times 10^8 / (\lambda c) \text{ E}$
Energy	J	$(1/\lambda) \text{ E}$
force	kg·m/s ²	$3.16153 \times 10^{-26} / (\lambda^2 \hbar c) \text{ E}^2$
temperature	K	$1.38065 \times 10^{-23} / (\lambda k_B) \text{ E}$
electric charge	C	$1.89032 \times 10^{18} \sqrt{\hbar c \epsilon_0}$
proton's charge	$1.60218 \times 10^{-19} \text{ C}$	$0.30286 \sqrt{\hbar c \epsilon_0}$
electric current	A	$1.99347 \times 10^{-16} \sqrt{c \epsilon_0} / (\lambda \sqrt{\hbar}) \text{ E}$
electric field	V/m	$1.67249 \times 10^{-44} / (\lambda^2 \hbar^{3/2} c^{3/2} \epsilon_0^{1/2}) \text{ E}^2$
magnetic field	T	$5.01398 \times 10^{-36} / (\lambda^2 \hbar^{3/2} c^{5/2} \epsilon_0^{1/2}) \text{ E}^2$

In NU, we define an energy unit E to corresponding to Joules in SI with a dimensionless ratio $\lambda = \text{E}/\text{J}$ or $1 \text{ E} = \lambda \text{ J}$. Note that E can span from MeV for microscopic processes to Joules for macroscopic ones. Then we obtain

$$\hbar c = 3.16152 \times 10^{-26} \text{ J} \cdot \text{m} = \frac{1}{\lambda} 3.16152 \times 10^{-26} \text{ E} \cdot \text{m}. \quad (2)$$

From the above relation we convert the unit of length in SI (meter) to NU

$$1 \text{ m} = 3.16303 \times 10^{25} \hbar c \lambda \text{ E}^{-1}. \quad (3)$$

Table I shows the conversion between SI and NU.

B. Conventions

RBG-Maxwell is a toolkit for relativistic plasma and can also be applied to non-relativistic plasma systems. The Latin letters in boldface denote the spatial and momentum three-vectors in Cartesian coordinates, e.g. $\mathbf{x} = (x, y, z)$ and $\mathbf{p} = (p_x, p_y, p_z)$. We choose the Greek letters such as μ to denote the time and space time index with $\mu = 0, 1, 2, 3$. For example, the four-momentum of particle with the rest mass m is denoted as $p^\mu = (p^0, \mathbf{p}) = (E_p/c, \mathbf{p})$ or $p_\mu = (p_0, -\mathbf{p}) = (E_p/c, -\mathbf{p})$, where $E_p = c\sqrt{|\mathbf{p}|^2 + m^2 c^2}$ is the energy of the particle. The convention of the metric tensor is $g^{\mu\nu} = \text{diag}(1, -1, -1, -1)$. The mass-shell condition is $m^2 c^2 = g^{\mu\nu} p_\mu p_\nu = p^\nu p_\nu$, where the Einstein's convention for summation is implied: repeated indices mean summation, $p^\nu p_\nu \equiv \sum_{\nu=0,1,2,3} p^\nu p_\nu$. Similar to the four-momentum p^μ , the four-coordinate is denoted as $x^\mu = (x^0, \mathbf{x}) = (ct, \mathbf{x})$. The Latin letter a denotes the particle species, such as electrons, protons, ions, etc.. We also use the Latin letter $i = 1, 2, 3$ to denote three spatial components, for example, x^i refers to $\mathbf{x} = (x^1, x^2, x^3) = (x, y, z)$.

III. RBG-MAXWELL FRAMEWORK

A. Single-particle distribution function

In relativistic kinetic theory, the single-particle distribution function $f_a(t, \mathbf{x}, \mathbf{p})$ for the particle species a in phase space is defined as

$$f_a(t, \mathbf{x}, \mathbf{p}) = \frac{\Delta N_a}{\Delta V_{\text{phase}}} = \frac{\Delta N_a}{\Delta x^3 \Delta p^3}, \quad (4)$$

where ΔN_a is the number of particles in the phase-space volume $\Delta V_{\text{phase}} = \Delta x^3 \Delta p^3$. In Eq. (4), all particles in the volume ΔV_{phase} are labeled by the same \mathbf{x} and \mathbf{p} . From $f_a(t, \mathbf{x}, \mathbf{p})$, we can obtain the particle number density $n_a(t, \mathbf{x})$

and the particle number $N_a(t)$ for the particle species a ,

$$\begin{aligned} n_a(t, \mathbf{x}) &= \int d^3\mathbf{p} f_a(t, \mathbf{x}, \mathbf{p}), \\ N_a(t) &= \int d^3\mathbf{x} n_a(t, \mathbf{x}), \end{aligned} \quad (5)$$

as well as the particle current density

$$j_a(t, \mathbf{x}) = \int d^3\mathbf{p} \mathbf{v} f_a(t, \mathbf{x}, \mathbf{p}), \quad (6)$$

with $\mathbf{v} = \mathbf{p}/p_0 = c\mathbf{p}/E_p$ being the relativistic velocity for the particle species a . We can obtain the total quantities by summation over the particle species a

$$n(t, \mathbf{x}) = \sum_a n_a(t, \mathbf{x}), \quad N(t) = \sum_a N_a(t), \quad j(t, \mathbf{x}) = \sum_a j_a(t, \mathbf{x}). \quad (7)$$

The particle number conservation equation reads

$$\frac{\partial n(t, \mathbf{x})}{\partial t} + \nabla \cdot j(t, \mathbf{x}) = 0. \quad (8)$$

The total energy-momentum tensor can be obtained via

$$T^{\mu\nu}(x) = \sum_a c \int \frac{d^3\mathbf{p}}{p^0} p^\mu p^\nu f_a(t, \mathbf{x}, \mathbf{p}), \quad (9)$$

where $T^{00}(x)$ is the energy density, $T^{0k}(x) = T^{k0}(x)$ with $k = 1, 2, 3$, is the momentum density (energy flux across the surface perpendicular to the k -direction), and T^{ij} with $i, j = 1, 2, 3$, is the momentum flux in the i -th component across the surface perpendicular to the j -direction. In particular, $T^{ii}(x)$ is called the normal stress, and $T^{ij}(x)$ with $i \neq j$ is called the shear stress. Then the energy-momentum conservation without EM fields can be expressed as

$$\partial_\mu T^{\mu\nu}(x) = 0, \quad (10)$$

where a summation over μ is implied. Other quantities, such as the electrical conductivity, the shear and bulk viscosity, can be obtained from single-particle distribution functions similarly.

In many systems such as hydro-magneto fluids, we often use the single-particle distribution in local thermal equilibrium such as the Maxwell-Boltzmann distribution

$$f_a^{\text{LTE}}(t, \mathbf{x}, E_p) \sim \exp\left[-\frac{E_p - \mu_a}{k_B T(t, \mathbf{x})}\right], \quad (11)$$

where μ is the chemical potential for the particle species a , and $T(t, \mathbf{x})$ is the local temperature. The off-equilibrium distribution functions can be obtained by solving the BE as shown later.

B. Coupled Boltzmann-Maxwell equations

The BE describes the evolution of the particle's phase space distribution in a particle system from an off-equilibrium state to the equilibrium state. The BE is just the equation that the rate of the variation in the phase space distribution function is caused by particle collisions. For the particle species a with the distribution $f_a(t, \mathbf{x}, \mathbf{p})$, the BE reads

$$\frac{df_a(t, \mathbf{x}, \mathbf{p})}{dt} = C[f_a(t, \mathbf{x}, \mathbf{p})], \quad (12)$$

where $C[f_a(t, \mathbf{x}, \mathbf{p})]$ is the collision term and df_a/dt in the left-hand-side is given by

$$\begin{aligned} \frac{df_a(t, \mathbf{x}, \mathbf{p})}{dt} &= \frac{\partial f_a(t, \mathbf{x}, \mathbf{p})}{\partial t} + \frac{\partial \mathbf{x}}{\partial t} \cdot \nabla_{\mathbf{x}} f_a(t, \mathbf{x}, \mathbf{p}) + \frac{\partial \mathbf{p}}{\partial t} \cdot \nabla_{\mathbf{p}} f_a(t, \mathbf{x}, \mathbf{p}) \\ &= \frac{\partial f_a(t, \mathbf{x}, \mathbf{p})}{\partial t} + \mathbf{v} \cdot \nabla_{\mathbf{x}} f_a(t, \mathbf{x}, \mathbf{p}) + \mathbf{F} \cdot \nabla_{\mathbf{p}} f_a(t, \mathbf{x}, \mathbf{p}), \end{aligned} \quad (13)$$

where $\partial\mathbf{x}/\partial t = \mathbf{v}$ and $\partial\mathbf{p}/\partial t = \mathbf{F}$ are respectively the effective velocity and force of the particle. $\nabla_{\mathbf{x}}$ and $\nabla_{\mathbf{p}}$ are the differential operators in coordinate and momentum space respectively. One can obtain $\partial\mathbf{x}/\partial t$ and $\partial\mathbf{p}/\partial t$ from the equation of motion of the particle. The terms proportional to $\partial\mathbf{x}/\partial t$ and $\partial\mathbf{p}/\partial t$ in Eq. (13) are usually called the drift and Vlasov terms, respectively.

The collision term describes short-range particle scatterings which can be calculated from the first principle such as quantum theory. In a plasma systems, the force is the long-range EM force, $\mathbf{F} = Q_a(\mathbf{E} + \mathbf{v}_a \times \mathbf{B})$, where Q_a is the electric charge of the particle species a , and \mathbf{E} and \mathbf{B} are the electric and magnetic fields acting on the particle, respectively. If there are no collisions among particles, i.e. the collision term is zero, the BE is called the Vlasov equation. It describes the time evolution of the collisionless system of charged particles in the long-range EM field. The EM field can be solved from Maxwell equations,

$$\begin{aligned}\nabla \times \mathbf{B} &= \frac{1}{c^2} \frac{\partial \mathbf{E}}{\partial t} + \frac{1}{c^2 \epsilon_0} \mathbf{J} \\ \nabla \times \mathbf{E} &= -\frac{\partial \mathbf{B}}{\partial t} \\ \nabla \cdot \mathbf{B} &= 0 \\ \nabla \cdot \mathbf{E} &= \frac{\rho}{\epsilon_0},\end{aligned}\tag{14}$$

where ϵ_0 and c can take arbitrary values in NU. In the above equations, ρ is the electric charge density, \mathbf{J} is the electric current density, and they are related to the particle's distribution functions solved from the BE

$$\begin{aligned}\rho &= \sum_a \int d^3\mathbf{p} f_a(t, \mathbf{x}, \mathbf{p}) Q_a, \\ \mathbf{J} &= \sum_a \int d^3\mathbf{p} f_a(t, \mathbf{x}, \mathbf{p}) Q_a \mathbf{v}_a.\end{aligned}\tag{15}$$

C. Collision term in BE

In this subsection, we discuss the construction of the collision term. The collision term can be expressed as momentum integrals for the binary collision (with the momentum setup) $a(\mathbf{k}_1) + b(\mathbf{k}_2) \rightarrow c(\mathbf{k}_3) + d(\mathbf{p})$ for particles a, b, c , and d

$$\begin{aligned}C_{ab \leftrightarrow cd} &\equiv \int \prod_{i=1}^3 d^3\mathbf{k}_i [f_{\mathbf{k}_1}^a f_{\mathbf{k}_2}^b F_{\mathbf{k}_3}^c F_{\mathbf{p}}^d - F_{\mathbf{k}_1}^a F_{\mathbf{k}_2}^b f_{\mathbf{k}_3}^c f_{\mathbf{p}}^d], \\ &\times \delta^{(4)}(k_1 + k_2 - k_3 - p) \frac{\hbar^2 c |M_{ab \leftrightarrow cd}|^2}{64\pi^2 k_1^0 k_2^0 k_3^0 p^0},\end{aligned}\tag{16}$$

where $M_{ab \leftrightarrow cd}$ is the invariant matrix element which can be obtained from microscopic theories such as quantum theory. If microscopic degree of freedoms (DOF) are involved such as spin and color in Quantum Chromodynamics [64, 65], an average over the DOF in the initial state and a sum over the DOF in the final state are implied in $M_{ab \leftrightarrow cd}$, and a sum over the DOF of the distribution function is also implied. The delta function in Eq. (16)

$$\begin{aligned}\delta^{(4)}(k_1 + k_2 - k_3 - p) &= \delta^{(3)}(\mathbf{k}_1 + \mathbf{k}_2 - \mathbf{k}_3 - \mathbf{p}) \\ &\times \delta(k_1^0 + k_2^0 - k_3^0 - p^0),\end{aligned}\tag{17}$$

ensures the energy and momentum conservation in the binary collision. The quantum correction

$$F_{\mathbf{p}}^d \equiv 1 + \theta \bar{n}(t, \mathbf{x}, \mathbf{p}),\tag{18}$$

where $\theta = \pm 1, 0$ for the Bose-Einstein, Fermi-Dirac, and Boltzmann statistics, respectively. The dimensionless quantity $\bar{n}(t, \mathbf{x}, \mathbf{p}) = (2\pi\hbar)^3 f(t, \mathbf{x}, \mathbf{p})/g$ is called the occupation number with g being the number of DOF. For electrons, we take $g = 2$ for the spin DOF; for photon or X-ray, we take $g = 1$; for quarks and gluons, we take $g = 6$ and $g = 16$, respectively.

We note that the collision term (16) is only valid when the momenta of colliding particles are independent of their positions and are uncorrelated before collisions. In history, the assumption is called by Boltzmann as the ‘‘Stosszahlansatz’’ (molecular chaos hypothesis) [66, 67]. Without such an assumption, the correlation between colliding

particles have to be considered instead of using $f_{\mathbf{k}_1}^a f_{\mathbf{k}_2}^b$ in Eq. (16). The Stosszahlansatz is deeply related to the Boltzmann's H-theorem [68, 69].

In a plasma system, there are some different collisions. For example, a photon may collide with a hydrogen atom to make it ionized, i.e. $\gamma + \text{H} \rightarrow e^- + \text{H}^+$. Its reverse reaction is the combination of an electron and a hydrogen ion to make a hydrogen atom with emission of a photon: $e^- + \text{H}^+ \rightarrow \text{H} + \gamma$. The Hydrogen atom may exchange an electron with another ion, i.e., $\text{H} + \text{H}^+ \rightarrow \text{H} + \text{H}^+$. Meanwhile, a hydrogen ion can collide with one another, i.e., $\text{H}^+ + \text{H}^+ \rightarrow \text{H}^+ + \text{H}^+$. So the collision term for H^+ is

$$C[f_{\text{H}^+}(t, \mathbf{x}, \mathbf{p})] = \left[\frac{1}{2} C_{\text{H}^+ + \text{H}^+ \rightarrow \text{H}^+ + \text{H}^+} + C_{\gamma + \text{H} \rightarrow \text{H}^+ + e^-} + C_{\text{H} + \text{H}^+ \rightarrow \text{H} + \text{H}^+} \right]. \quad (19)$$

Since all H^+ are indistinguishable, we have introduced the symmetry factor 1/2 in front of the term $C_{\text{H}^+ + \text{H}^+ \rightarrow \text{H}^+ + \text{H}^+}$ when all incident particles are of the same type (species).

D. Cross section and matrix element

Sometimes we only have the measured cross sections in experiments instead of matrix elements. So it is necessary to find the relationship between the cross section and the matrix element.

For a two-to-two scattering process $ab \leftrightarrow cd$, the differential cross section $d\sigma$ is defined through the differential probability per unit time

$$\begin{aligned} d\omega &= c(2\pi\hbar)^4 \delta^{(4)}(k_1 + k_2 - k_3 - p) |M_{ab \leftrightarrow cd}|^2 V \\ &\times \frac{1}{2E_1 2E_2 2E_3 2E_p} \frac{\hbar^4 c^4}{V^4} \frac{V d^3 \mathbf{k}_3}{(2\pi\hbar)^3} \frac{V d^3 \mathbf{p}}{(2\pi\hbar)^3} \\ &= \frac{cI}{k_1^0 k_2^0 V} d\sigma, \end{aligned} \quad (20)$$

where V is the space volume, $k_1 = (E_1, \mathbf{k}_1)$ and $k_2 = (E_2, \mathbf{k}_2)$ are the energy-momenta of incoming particles respectively, and $k_3 = (E_3, \mathbf{k}_3)$ and $k_4 = (E_4, \mathbf{k}_4)$ are the energy-momenta of outgoing particles respectively. The invariant flux I of incoming particles is defined as

$$I(k_1^\mu, k_2^\mu) = \sqrt{(k_1^\mu k_{2,\mu})^2 - m_1^2 m_2^2 c^4}. \quad (21)$$

Combining Eqs. (20) and (21), we obtain the differential cross section in the Lab frame for the particle d ,

$$\frac{d\sigma}{d\Omega} \Big|_{a(\mathbf{k}_1) + b(\mathbf{k}_2) \leftrightarrow c(\mathbf{k}_3) + d(\mathbf{p})} = \frac{\hbar^2 |M_{ab \leftrightarrow cd}|^2 |\mathbf{p}|}{64\pi^2 k_3^0 I(k_1^\mu, k_2^\mu)}. \quad (22)$$

E. Jefimenko's equations

As a general solution to Maxwell equations, Jefimenko's equations [70] can be directly derived from the retarded potential in Maxwell equations [71, 72],

$$\begin{aligned} \mathbf{E}(\mathbf{r}, t) &= \frac{1}{4\pi\epsilon_0} \int \left[\frac{\mathbf{r} - \mathbf{r}'}{|\mathbf{r} - \mathbf{r}'|^3} \rho(\mathbf{r}', t_r) + \frac{\mathbf{r} - \mathbf{r}'}{|\mathbf{r} - \mathbf{r}'|^2} \frac{1}{c} \frac{\partial \rho(\mathbf{r}', t_r)}{\partial t} \right. \\ &\quad \left. - \frac{1}{|\mathbf{r} - \mathbf{r}'|} \frac{1}{c^2} \frac{\partial \mathbf{J}(\mathbf{r}', t_r)}{\partial t} \right] d^3 \mathbf{r}', \end{aligned} \quad (23)$$

$$\begin{aligned} \mathbf{B}(\mathbf{r}, t) &= -\frac{1}{4\pi\epsilon_0 c^2} \int \left[\frac{\mathbf{r} - \mathbf{r}'}{|\mathbf{r} - \mathbf{r}'|^3} \times \mathbf{J}(\mathbf{r}', t_r) \right. \\ &\quad \left. + \frac{\mathbf{r} - \mathbf{r}'}{|\mathbf{r} - \mathbf{r}'|^2} \times \frac{1}{c} \frac{\partial \mathbf{J}(\mathbf{r}', t_r)}{\partial t} \right] d^3 \mathbf{r}', \end{aligned} \quad (24)$$

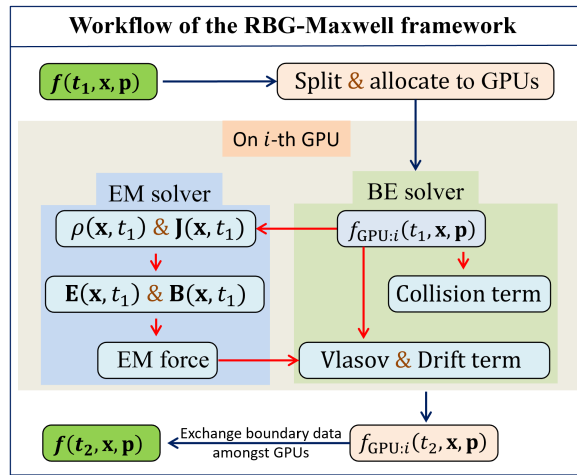


Figure 1: Schematic of the workflow of the RBG-Maxwell framework. BE (Boltzmann) and EM (EM) solvers are revised from our previous packages JefiGPU [52] and RBG[57]. At each time step, BE solver provides the charge and current densities to the EM solver, and EM solver gives the EM forces exerted on the particles.

where $t_r = t - |\mathbf{r} - \mathbf{r}'|/c$ is the retarded time, \mathbf{E} and \mathbf{B} are the electric and magnetic fields at the space-time point (\mathbf{r}, t) , respectively, and ρ and \mathbf{J} are the charge and current densities at the space-time point (\mathbf{r}', t_r) , respectively.

The integration form in Eqs. (23) and (24) has some merits. First, different from the finite-difference time-domain (FDTD) method [73], Jefimenko's equations do not rely on boundary conditions. In the FDTD method, choosing proper boundary conditions is a complex and technical sub-field [74–78]. A slight change of boundary conditions can lead to different EM fields [79]. The integration form, on the other hand, merely relies on the source terms, i.e. time-dependent charge and current densities $\rho(\mathbf{r}', t_r)$ and $\mathbf{J}(\mathbf{r}', t_r)$. Once one obtains $\rho(\mathbf{r}', t_r)$ and $\mathbf{J}(\mathbf{r}', t_r)$ from the BE through Eq. (15), it is much easier to put the calculation of $\mathbf{E}(\mathbf{r}, t)$ and $\mathbf{B}(\mathbf{r}, t)$ through Jefimenko's equations (23) and (24) on GPU clusters than through Maxwell equations. However, there is a cost to pay in using the integration form. In the FDTD method, $\mathbf{E}(\mathbf{r}, t)$ and $\mathbf{B}(\mathbf{r}, t)$ in the vicinity $(\mathbf{r} \pm d\mathbf{r}, t \pm dt)$ are needed, while in Eqs. (23) and (24) the sources $\rho(\mathbf{r}', t_r)$ and $\mathbf{J}(\mathbf{r}', t_r)$ at all previous time in the entire computational domain are needed.

Moreover, the integrations in Jefimenko's equations are always well-defined except there is a divergence at $\mathbf{r} = \mathbf{r}'$. The near-source divergence has its profound physical origins [50, 51]. The usual treatment of the singularity is to adopt the finite size of the spatial grid as a cut-off, $|\mathbf{r} - \mathbf{r}'|_{\text{cut-off}} = \sqrt{(dx)^2 + (dy)^2 + (dz)^2}$. When $|\mathbf{r} - \mathbf{r}'| < |\mathbf{r} - \mathbf{r}'|_{\text{cut-off}}$ we can set $\rho(\mathbf{r}', t_r) = \mathbf{J}(\mathbf{r}', t_r) = 0$, so the divergence is removed. In this case, the EM field in a specific grid can only be generated by the charge and current densities in other grids.

IV. ALGORITHMS

The RBG-Maxwell framework is a first-principle based plasma toolkit. In the current version, limited by the molecular chaos hypothesis [66, 67], it can only deal with dilute plasma systems at the weak coupling limit. Similar to most plasma toolkits, it contains two main blocks in general, as shown in Fig. 1, the BE solver for the phase space distribution functions and the EM field solver for the EM fields generated by these distributions.

As a stable solution to Maxwell equations, Jefimenko's equations give the EM fields from charge and current densities provided by distribution functions. Given the distribution $f(t_1, \mathbf{x}, \mathbf{p})$ and the external force $\mathbf{F}(t_1, \mathbf{x}, \mathbf{p})$ depending on the EM field at a previous time t_1 , the BE solver gives $f(t_2, \mathbf{x}, \mathbf{p})$ at a later time t_2 . In the BE solver, the collision term $\mathcal{C}[f]$ is performed in the Monte Carlo approach with the symmetric sampling method [57]. The drift and Vlasov terms $\mathbf{v}_a \cdot \nabla_{\mathbf{x}}$ and $\mathbf{F} \cdot \nabla_{\mathbf{p}}$ are differentiated by the first or second order finite difference method. Then $f(t_2, \mathbf{x}, \mathbf{p})$ is input to Jefimenko's equations to obtain the EM fields at t_2 from which a new cycle is started. Therefore the RBG-Maxwell framework is a fully consistent algorithm for the coupled relativistic Boltzmann-Maxwell equations.

All modules are implemented by Python and are made heavily parallel on GPU clusters, which makes a fast solver to the coupled equations. All quantities in RBG-Maxwell are consistently defined on GPU clusters via the Python package CuPy [80, 81] (CuPy is an implementation of NumPy-compatible multi-dimensional array on CUDA). The CUDA kernel functions are written with the Python package Numba [82, 83] (an open source JIT compiler that translates a subset of Python and NumPy code into fast machine code).

A. Boltzmann Equation solver

The BE solver is an updated version of our previous work – Relativistic Boltzmann equations on GPUs (RBG) [57]. The algorithm for the calculation of the collision term is the same as in RBG, while other parts are redesigned to fit the RBG-Maxwell framework. In the calculation of distribution functions, we must always keep them non-negative, otherwise, the algorithm will quickly blow up and lead to wrong solutions. In order to preserve their positivity, we need to revise some of existing positivity preserving schemes accordingly. First and second order positivity preserving upwind difference schemes are adopted to approximate spatial gradients, and first order positivity preserving upwind difference scheme is used to approximate momentum gradients. Other functionalities, such as non-negative distribution functions and flux limiters, are also included in the framework.

For numerical convenience, we rewrite Eqs. (12) and (13) into three equations

$$\frac{1}{3} \frac{\partial f_a(t, \mathbf{x}, \mathbf{p})}{\partial t} + \mathbf{v} \cdot \nabla_{\mathbf{x}} f_a(t, \mathbf{x}, \mathbf{p}) = 0, \quad (25)$$

$$\frac{1}{3} \frac{\partial f_a(t, \mathbf{x}, \mathbf{p})}{\partial t} + \mathbf{F} \cdot \nabla_{\mathbf{p}} f_a(t, \mathbf{x}, \mathbf{p}) = 0, \quad (26)$$

$$\frac{1}{3} \frac{\partial f_a(t, \mathbf{x}, \mathbf{p})}{\partial t} = C[f_a(t, \mathbf{x}, \mathbf{p})]. \quad (27)$$

Therefore, solving the BE is equivalent to solving above three equations.

1. Drift term

We use the first and second order finite difference methods in calculating distribution functions. For a fast and smooth evolution of distribution functions, one is advised to use the first order upwind difference scheme, but with the problem of significant diffusion [84–86] which is problematic for relativistic plasma systems since it breaks causality to a large extent. To overcome such a problem, we have to employ the second order flux-limited method to suppress the diffusion.

First order scheme. We adopt the unconditionally positivity preserving finite difference scheme [87, 88] (UPFD) to approximate the gradients of drift terms. The usual treatment of gradients is

$$\begin{aligned} v_x \frac{\partial f_a(t, x, y, z)}{\partial x} &= v_x \frac{f_a(t, x, y, z) - f_a(t, x - \Delta x, y, z)}{\Delta x} \quad (v_x > 0), \\ v_x \frac{\partial f_a(t, x, y, z)}{\partial x} &= v_x \frac{f_a(t, x + \Delta x, y, z) - f_a(t, x, y, z)}{\Delta x} \quad (v_x < 0). \end{aligned} \quad (28)$$

The upwind difference does not guarantee that $f_a(t + \Delta t, \mathbf{x})$ is always positive when updated via Eq. (25). To achieve positivity, we can make following replacements,

$$\begin{aligned} f_a(t, x, y, z) - f_a(t, x - \Delta x, y, z) &\rightarrow f_a(t + \Delta t, x, y, z) - f_a(t, x - \Delta x, y, z) \quad (v_x > 0), \\ f_a(t, x + \Delta x, y, z) - f_a(t, x, y, z) &\rightarrow f_a(t, x + \Delta x, y, z) - f_a(t + \Delta t, x, y, z) \quad (v_x < 0). \end{aligned} \quad (29)$$

Substituting Eq. (29) into Eq.(25) we obtain an explicit expression for always positive distributions

$$f_a(t + \Delta t, \mathbf{x}) = \frac{3\Delta x}{3|v_x|\Delta t + \Delta x} \left(\frac{1}{3} f_a(t, \mathbf{x}) + \frac{\Delta t |v_x|}{\Delta x} \begin{cases} f_a(t, x - \Delta x, y, z) & v_x > 0 \\ f_a(t, x + \Delta x, y, z) & v_x < 0 \end{cases} \right). \quad (30)$$

The same formula can be obtained in the y and z directions.

Second order scheme. As will be illustrated in Sec. V, the first order upwind difference scheme brings significant numerical diffusion. So we need to adopt the second order scheme to suppress the numerical diffusion. The method we use in the RBG-Maxwell framework is adapted from the positivity-preserving flux-limited method (PFL) [89].

For convenience, we use f_i^n to denote $f_a(t, \mathbf{x}, \mathbf{p})$, where n and $i = x, y, z$ represent time and spatial indices respectively. Following the PFL, Eq. (25) can be approximated by

$$\frac{1}{3} \frac{f_i^{n+1} - f_i^n}{\Delta t} + \sum_{i=x,y,z} \frac{F_{i+1/2} - F_{i-1/2}}{\Delta x_i} = 0, \quad (31)$$

where the convection flux is defined as

$$F_{i+1/2} = v_i^+ f_i^n + \frac{1}{2} \phi_{i+1/2}^+ (v_i^+ f_i^n - v_{i-1}^+ f_{i-1}^n) \\ + v_{i+1}^- f_{i+1}^n + \frac{1}{2} \phi_{i+1/2}^- (v_{i+1}^- f_{i+1}^n - v_{i+2}^- f_{i+2}^n). \quad (32)$$

Here a flux limiter ϕ is introduced in front of the difference terms. Its function is to decrease the value of the gradient and further suppress the numerical diffusion. The flux limiters take the following form

$$\phi_{i+\frac{1}{2}}^+ = \max \left(0, \min \left(1, \underbrace{\frac{v_{i+1}^+ f_{i+1}^n - v_i^+ f_i^n}{v_i^+ f_i^n - v_{i-1}^+ f_{i-1}^n}}_{\text{flux limiter for monotonicity preservation}}, \underbrace{\frac{2}{\max(\theta, (v_{i-1}^+ f_{i-1}^n - v_i^+ f_i^n)/v_i^+ f_i^n)}}_{\text{additional limiter for positivity preservation}} \right) \right), \\ \phi_{i+\frac{1}{2}}^- = \max \left(0, \min \left(1, \underbrace{\frac{v_i^- f_i^n - v_{i+1}^- f_{i+1}^n}{v_{i+1}^- f_{i+1}^n - v_{i+2}^- f_{i+2}^n}}_{\text{flux limiter for monotonicity preservation}}, \underbrace{\frac{2}{\max(\theta, (v_{i+2}^- f_{i+2}^n - v_{i+1}^- f_{i+1}^n)/v_{i+1}^- f_{i+1}^n)}}_{\text{additional limiter for positivity preservation}} \right) \right), \quad (33)$$

where a Total Variation Diminishing (TVD) [90, 91] limiter is used to preserve monotonicity and an additional limiter is adopted to preserve positivity. We set the parameter $\theta = 10^{-10}$ throughout the code.

Boundary conditions. In real cases, the particles can be either absorbed or reflected by the boundaries. For practical convenience, we introduce a positive parameter $\zeta(x, y, z)$ [$0 < \zeta(x, y, z) < 1$] to describe the reflective probability and then $1 - \zeta(x, y, z)$ represents the absorber probability at the boundaries.

2. Vlasov term

First order scheme. Similar to the drift term, we also apply the UPDF scheme to the Vlasov term,

$$f_a(t + \Delta t, \mathbf{p}) = \frac{3\Delta p_x}{3|F_x|\Delta t + \Delta p_x} \left(\frac{1}{3} f_a(t, \mathbf{p}) + \frac{\Delta t |F_x|}{\Delta p_x} \begin{cases} f_a(t, p_x - \Delta p_x, p_y, p_z) & F_x > 0 \\ f_a(t, p_x + \Delta p_x, p_y, p_z) & F_x < 0 \end{cases} \right). \quad (34)$$

The same formula can be obtained in the y and z directions.

Boundary conditions. Given that the distribution functions invariably approach zero at high momentum values, we can utilize periodic boundaries for differentiation across all momentum dimensions. It's important to underscore that this implementation will maintain the conservation of momentum intact, despite any variations.

3. Collision term

The collision term presents the most significant challenge in the numerical implementation of the Boltzmann Equation, as it necessitates high-dimensional integration at each phase space grid. For binary collisions, it is crucial to integrate the delta function prior to any additional numerical implementations. To resolve the delta function, we adopt the technique of integration over $d^3 \mathbf{k}_2$ and dk_{1z} as described by Ref. [57] in Eq. (16). For a more detailed explanation, please refer to Appendix VII,

$$\int \prod_{i=1}^3 d^3 \mathbf{k}_i \delta^{(4)}(k_1 + k_2 - k_3 - p) \\ = \int d^3 \mathbf{k}_3 dk_1^x dk_1^y \sum_{i=\pm} \frac{1}{|J(k_{1z}^i)|}, \quad (35)$$

where the Jacobin

$$J(k_{1z}^\pm) = \frac{k_{1z}^\pm}{(k_1^0)^\pm} - \frac{-k_{1z}^\pm + k_{3z} + p_z}{(k_2^0)^\pm}, \\ k_{1z}^\pm = \text{Root}[k_1^0 + k_2^0 - k_3^0 - p^0 = 0]. \quad (36)$$

There are two roots for k_{1z} from the equation $k_1^0 + k_2^0 - k_3^0 - p^0 = 0$, and k_{1z} has the form of $k_{1z}^\pm \equiv \frac{C1 \pm \sqrt{H}}{C2}$, where $C1, C2$, and H are functions of k_1^x, k_1^y and \mathbf{k}_3 . The explicit expressions of $C1, C2$, and H are given in Appendix VII. Substituting Eq. (35) into Eq. (16), we obtain the 5-dimensional collision integral

$$C_{ab \rightarrow cd} = \int d^3 \mathbf{k}_3 dk_1^x dk_1^y \frac{\hbar^2 c |M_{ab \leftrightarrow cd}|^2}{64 \pi^2 k_1^0 k_2^0 k_3^0 p^0} \sum_{i=\pm} \frac{1}{|J(k_{1z}^i)|} \times [f_{\mathbf{k}_1}^a f_{\mathbf{k}_2}^b F_{\mathbf{k}_3}^c F_{\mathbf{p}}^d - F_{\mathbf{k}_1}^a F_{\mathbf{k}_2}^b f_{\mathbf{k}_3}^c f_{\mathbf{p}}^d]. \quad (37)$$

Eq. (37) can be evaluated numerically by the Direct Monte Carlo (DMC) method[92, 93]. In RBG-Maxwell, the 5-dimensional integration is performed by the GPU package ZMCintegral[48, 49].

B. EM field solver

A distinctive characteristic of a plasma system is the emergence of (classical) Electromagnetic (EM) fields within the calculation domains. These EM fields can originate from two potential sources: the fluctuating or constant ambient fields generated by other systems, and the fields produced by the motion of the plasma particles. A uniform GPU-based approach to both the EM fields and the particle transport necessitates a stable and concise solution to Maxwell equations. In our quest for complete consistency in the relativistic limit, we have opted for the integral form (specifically, Jefimenko's equation) of the EM fields as opposed to the FDTD method.

For numerical convenience, we discretize Eqs. (23) and (24) as

$$\mathbf{E}(\mathbf{r}, t) = \frac{1}{4\pi\epsilon_0} d\Omega' \sum_{i,j,k} \left[\frac{\mathbf{r} - \mathbf{r}'_{i,j,k}}{|\mathbf{r} - \mathbf{r}'_{i,j,k}|^3} \rho(\mathbf{r}'_{i,j,k}, t_r) + \frac{\mathbf{r} - \mathbf{r}'_{i,j,k}}{|\mathbf{r} - \mathbf{r}'_{i,j,k}|^2} \frac{1}{c} \frac{\rho(\mathbf{r}'_{i,j,k}, t_r) - \rho(\mathbf{r}'_{i,j,k}, t_r - dt)}{dt} - \frac{1}{|\mathbf{r} - \mathbf{r}'_{i,j,k}|} \frac{1}{c^2} \frac{\mathbf{J}(\mathbf{r}'_{i,j,k}, t_r) - \mathbf{J}(\mathbf{r}'_{i,j,k}, t_r - dt)}{dt} \right] \quad (38)$$

$$\mathbf{B}(\mathbf{r}, t) = -\frac{1}{4\pi\epsilon_0 c^2} d\Omega' \sum_{i,j,k} \left[\frac{\mathbf{r} - \mathbf{r}'_{i,j,k}}{|\mathbf{r} - \mathbf{r}'_{i,j,k}|^3} \times \mathbf{J}(\mathbf{r}'_{i,j,k}, t_r) + \frac{\mathbf{r} - \mathbf{r}'_{i,j,k}}{|\mathbf{r} - \mathbf{r}'_{i,j,k}|^2} \times \frac{1}{c} \frac{\mathbf{J}(\mathbf{r}'_{i,j,k}, t_r) - \mathbf{J}(\mathbf{r}'_{i,j,k}, t_r - dt)}{dt} \right] \quad (39)$$

$$t_r = t - \frac{|\mathbf{r} - \mathbf{r}'_{i,j,k}|}{c}, \quad (40)$$

where index $i \in \{1, 2, \dots, n_x\}$, $j \in \{1, 2, \dots, n_y\}$, $k \in \{1, 2, \dots, n_z\}$ and volume element $d\Omega' = dx' dy' dz'$. n_x, n_y and n_z denote the number of spatial grids used in the calculation. It's crucial to acknowledge that \mathbf{r} and $\mathbf{r}'_{i,j,k}$ can be defined in distinct regions. The calculation domain of the EM solver comprises two areas: the source region (which contains $\mathbf{r}'_{i,j,k}$) and the observation region (which houses \mathbf{r}). The source region is the domain where the single particle distribution function is defined. The observation region, on the other hand, may envelop the source region or encompass other domains of interest. For instance, suppose a plasma clump is produced in a laboratory, and we're interested in the electromagnetic field it generates outside the lab. In this case, the source region pertains to the cavity containing the plasma, and the observation region includes both the source region and the area outside the lab.

The superiority of our method over the more efficient FDTD approach manifests in two ways in RBG-Maxwell. Firstly, the integration method is more stable compared to the FDTD approach. During numerical calculations, integrations are less likely to yield infinities, which significantly simplifies the GPU implementation. Secondly, the FDTD approach is local, meaning the EM fields are determined only by the surrounding fields. If the EM fields in the adjacent grids are not updated accurately, the errors will accumulate over subsequent time steps. This is particularly crucial in ultra-relativistic scenarios. On the contrary, the Jefimenko equations are non-local - the EM fields are calculated considering all possible grids across the entire spatial domain. Consequently, they are less sensitive to the conditions of nearby grids compared to the FDTD approach.

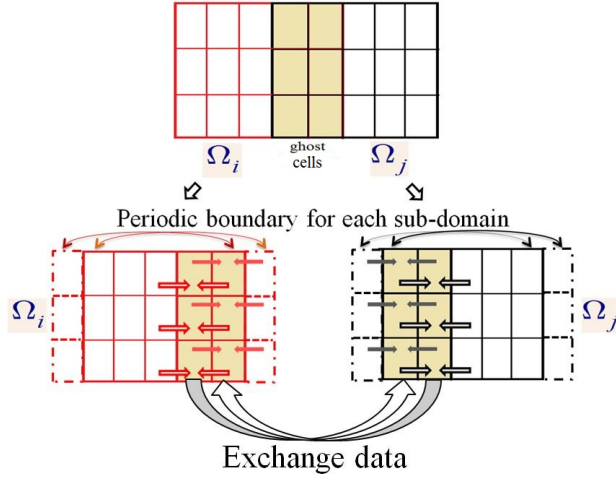


Figure 2: Illustration of the ghost cells between two overlapping regions. The ghost cells between Ω_i (depicted by the red grid) and Ω_j (illustrated by the black grid) are shaded in yellow. In the first-order upwind difference, the value of the distribution function at a spatial grid is influenced by its nearest grids, as demonstrated by the mutually pointing arrows. Given that we employ periodic boundaries for each sub-domain, the distribution functions at the edges of the sub-domain may not be accurate (as indicated by the regions pointed out by the two mutually pointing solid arrows).

C. Parallelization among clusters

The essence of parallelization lies in minimizing the data exchange volume among the GPU cards. The parallelization module in RBG-Maxwell handles two components: the parallelization of single particle distribution functions and that of electromagnetic fields. For distribution functions, we partition the spatial domain into multiple sub-domains, which share boundaries with each other. At each time step, only the shared boundaries of the distribution functions are exchanged among the GPU cards. For the electromagnetic fields \mathbf{E} and \mathbf{B} , the distribution functions on each GPU card yield the electric charge density ρ and the electric current density \mathbf{J} . On each GPU card, the EM fields produced by ρ and \mathbf{J} for the entire spatial domain are calculated and distributed to the respective GPU cards. Hence, only the computed EM fields are exchanged among the GPU cards, while the source terms are retained on the GPU cards throughout the simulation.

These functionalities are enabled by the Python package Ray[94, 95], which provides a straightforward and universal API for developing distributed applications.

1. Ghost Cells in spatial domain

The spatial domain is segmented into numerous sub-domains, dependent on the total number of available GPU cards. To enhance clarity, we utilize the symbol Ω to represent the domain of the spatial region. In a GPU cluster comprising M GPUs, Ω is partitioned into $\Omega_1, \Omega_2, \dots, \Omega_M$ sub-domains, each corresponding to a separate GPU card.

The distribution function of a spatial grid located at the edges of a sub-domain is influenced by its two adjacent grids - one of these adjacent grids replicates from the opposite edge (regions connected by the arc-arrows in Fig. 2). We apply the concept of ghost cells (as explored by Refs. [96, 97]), a technique broadly employed for parallel computations. Ghost cells are designated as the overlapped regions between two adjacent sub-domains, as demonstrated in Fig. 2. After each time step, the values of the distribution functions at the edges are updated by exchanging data with the neighboring sub-domains.

2. Parallelization of EM fields

The division of the spatial domain for the electromagnetic (EM) fields mirrors that of the distribution functions. On each GPU card (consequently each sub-domain Ω_i where i is in the set $\{1, 2, \dots, M\}$), the integrations of the distribution functions yield the electric current density \mathbf{J} and the electric charge density ρ . The calculated \mathbf{J} and ρ at each time snapshot will be preserved in the GPU memory. Following the formulation of the Jefimenko's equations

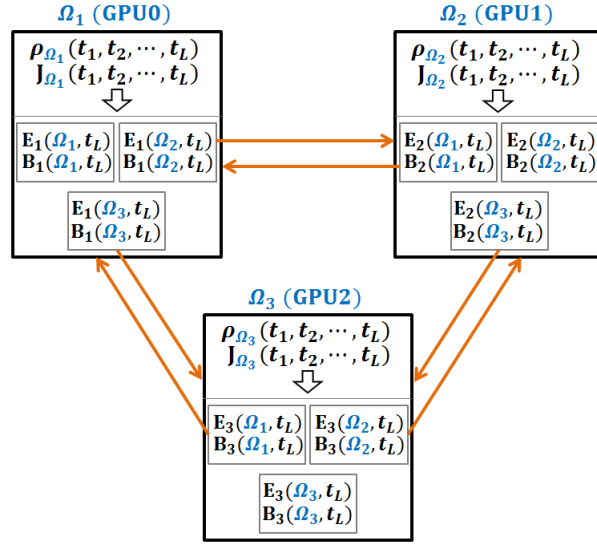


Figure 3: Parallelization scheme of the electromagnetic fields on GPUs. The sources \mathbf{J} and ρ on each card give the EM fields on all GPU cards. The obtained EM fields are distributed to other GPU cards instantly.

(38)~(40), \mathbf{J} and ρ in region Ω_i contribute to the EM fields in $\Omega_1, \Omega_2, \dots, \Omega_M$.

In Fig. 3, we illustrate the parallelization scheme for a case comprising three sub-domains $\Omega = \{\Omega_1, \Omega_2, \Omega_3\}$. The time sequence $\{t_1, t_2, \dots, t_L\}$ represents the evaluated time steps, with the current time step being denoted as t_L . The \mathbf{J} and ρ at each time snapshot are preserved in the GPU memory, forming the sequences $\rho_{\Omega_i}(t_1, t_2, \dots, t_L)$ and $\mathbf{J}_{\Omega_i}(t_1, t_2, \dots, t_L)$ where Ω_i is a member of $\{\Omega_1, \Omega_2, \Omega_3\}$. Utilizing ρ_{Ω_i} and \mathbf{J}_{Ω_i} , the EM fields for sub-domains $\Omega_1, \Omega_2, \Omega_3$ can be calculated via Eqs. (38)~(40). The EM fields thus obtained on each GPU card are then transferred to the respective sub-domains. Throughout the evaluation process, only the EM fields at the time step t_L are exchanged. The resolution (or equivalently, the number of spatial grids) for each sub-domain Ω_i is constrained by the resolution of the Boundary Element (BE) solver. At the current stage, the number of grids for a BE solver on a single GPU card is approximately of size $[n_x, n_y, n_z, n_{p_x}, n_{p_y}, n_{p_z}] \simeq [10, 10, 10, 10, 10, 10]$. Therefore, the exchanged EM fields have a size of $[n_x, n_y, n_z] \simeq [10, 10, 10]$. With a GPU card boasting a few million cores, the exchanged EM fields can reach a size of $[n_x, n_y, n_z] \simeq [100, 100, 100]$, which equates to a few megabytes. Consequently, the volume of the exchanged EM fields is rather small.

In some cases, the plasma is restricted in a system while the interested EM fields is outside the plasma system. In these scenarios, each GPU card gives the EM fields for the interested regions following a similarly scheme as in Fig. 3.

V. VERIFICATION ON MULTI-GPUS

In this section, we will validate the RBG-Maxwell framework from three different perspectives. Firstly, we employ a simple model example to illustrate the evolution of particles and their respective electromagnetic fields. The resulting outcomes are then compared with the plasma toolkit, JefPIC. Secondly, we select a particle system composed of two species and confine these particles within a box. Over time, the particles engage in collisions and gradually transition into a thermal state. Lastly, we execute the code on eight GPU cards to assess the parallel performance. During all these tests, the absorbing boundary conditions are applied to all spatial boundaries.

1. Test of drift and Vlasov terms

We use a two dimensional (2D) pure electron plasma system to test the drift and Vlasov terms. The 2D domain is divided into many spatial grids with each grid having a size of $dx = dy = dz = 10^{-5}\text{m}$.

Difference between first and second order schemes. As depicted in Fig. 4, the grid numbers in the spatial domain are selected to be $n_x \times n_y \times n_z = 1 \times 251 \times 111$. A total of 31,250 electrons are uniformly dispersed across the shaded

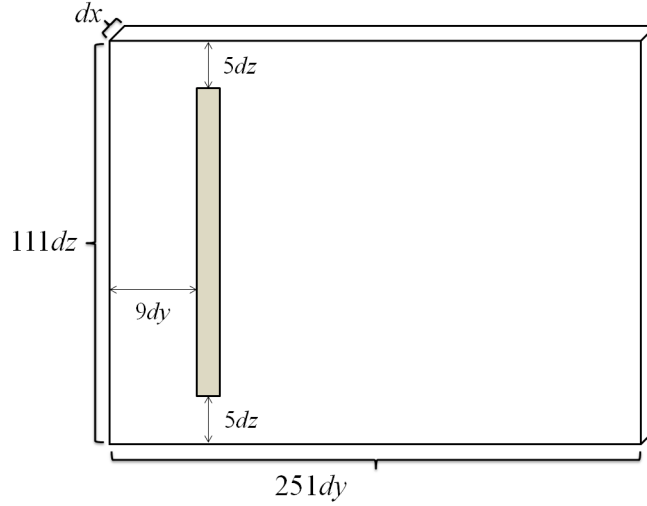


Figure 4: Schematic illustration of the initial configuration of the electron plasma for order comparison.

regions, each with a constant initial velocity of 1.87683×10^6 m/s. This initial setup corresponds to the distribution function

$$f_e(\mathbf{x}_i, \mathbf{p}_j, t_0) = \begin{cases} \frac{31250}{101dV} & \mathbf{x}_i \text{ in the shaded area \& } |\mathbf{p}_j| \leftrightarrow 1.87683 \times 10^6 \text{ m/s} \\ 0. & \text{elsewhere} \end{cases}, \quad (41)$$

where the phase grid volume $dV = dx dy dz dp_x dp_y dp_z$, and $|\mathbf{p}_i| \leftrightarrow 1.87683 \times 10^6$ m/s means the momentum grid $|\mathbf{p}_j|$ is obtained via the velocity 1.87683×10^6 m/s. $i \in \{1, \dots, M\}$ and $j \in \{1, \dots, N\}$ are the indices of the discretized spatial and momentum grids (suppose we have divided the entire phase space into $M \times N$ grids). To see the pure effects of the diffusion in drift term, we have neglected all the EM fields in the simulation. The same initial condition is also simulated by the package JefiPIC[52], which is based on the particle simulation method.

In Fig. 5, we present the acquired particle distributions in the $yo z$ plane. As no electromagnetic fields are present, the particles are anticipated to move along the y -axis. Due to the numerical diffusion inherent in the finite difference method, we observe significant diffusion in the first order scheme. The second order scheme exhibits less diffusion and is hence recommended for relativistic scenarios. Concurrently, the particle simulation method exhibits minimal diffusion effects, a reasonable outcome given its fine resolution in spatial coordinates. Generally, all three models yield acceptable simulation results. However, diffusion effects are expected to be suppressed when the electromagnetic fields are applied head-on (see detailed comparisons in Ref. [52]). The evaluation time for the first and second order schemes for 10,000 steps is approximately 162 and 168 seconds respectively, when performed on a single Tesla A 100 card.

Particle distributions and the electric fields The electrons are initially positioned at the central grid of the spatial domain. The 2D domain is segmented into 101×101 spatial grids, each with dimensions of $dx = dy = dz = 10^{-5}$ m. An observation point, located at [0-th, 25-th, 25-th] grids away from the center, monitors the time evolution of the electric field $E_y(t)$. This configuration is schematically depicted in Fig. 6. The velocities of the electrons follow a Gaussian distribution

$$f_e(p) = N_e \frac{1}{\sqrt{2\pi\sigma^2}} e^{-\frac{(p-p_{ave})^2}{2\sigma^2}}, \quad (42)$$

where the momentum $p = |\mathbf{p}|$, the average initial momentum $p_{ave} = m_e v_{ave} / \sqrt{1 - (v_{ave}/c)^2}$, and $v_{ave} = 1.87864 \times 10^6$ m/s, $\sigma = 0.2p_{ave}$. The normalization constant N_e is chosen such that $\int d\mathbf{p} f_e(p) = N$, where the total initial electron number $N = 31250$. For a smooth spatial distribution, the particles are distributed in the spatial coordinates following an exponential expression

$$f_e(x) = M_e e^{-x^2}, \quad (43)$$

where the variable $x = |\mathbf{x}|$, and the normalization constant M_e is chosen such that $\int d\mathbf{x} f_e(x) = 1$. Combining Eqs. (42) and (43), we obtain the initial distribution function of the electrons

$$f_e(\mathbf{x}, \mathbf{p}, t_0) = f_e(p) f_e(x), \quad (44)$$

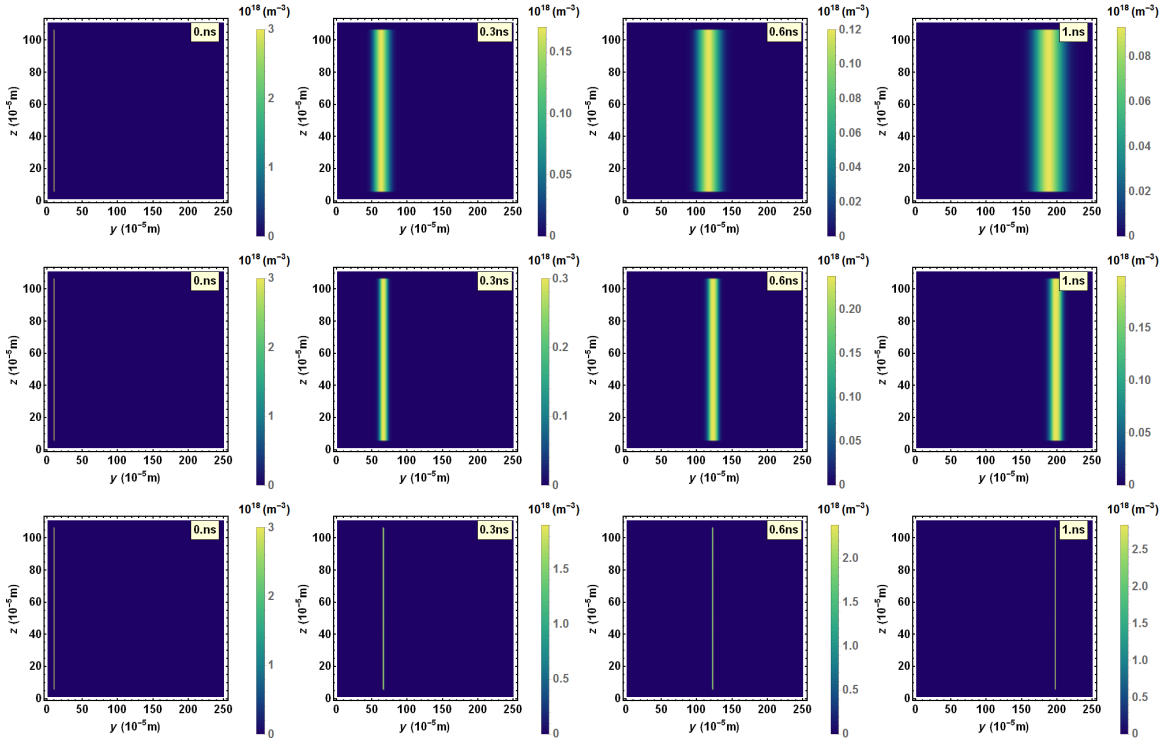


Figure 5: Effects of diffusion. All EM fields are set to be zero. The three lines correspond to the results from RBG-Maxwell 1st order, RBG-Maxwell 2ed order, and JefiPIC.

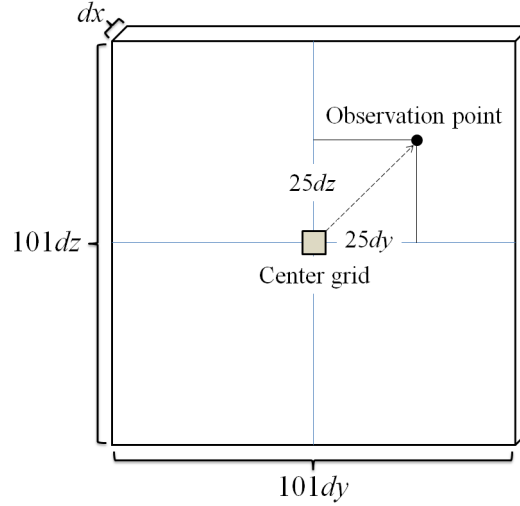


Figure 6: Schematic illustration of the initial configuration of the electron plasma for particle distributions and electric fields. The center grid is of size $dx \times dy \times dz$. $[0, 25, 25]$ grids away from the center grid, an observation point is chosen to record the electric field along the y direction.

where the initial total particle number is

$$\begin{aligned} \int d\mathbf{x} d\mathbf{p} f_e(\mathbf{x}, \mathbf{p}, t_0) &= \int d\mathbf{x} d\mathbf{p} f_e(p) f_e(x) \\ &= N. \end{aligned} \quad (45)$$

Fig. 7 depicts the snapshots of the particle densities in the yo z plane. A similar model is also executed using JefiGPU (a particle simulator) to cross-validate our results. It is evident that the particle densities obtained by both

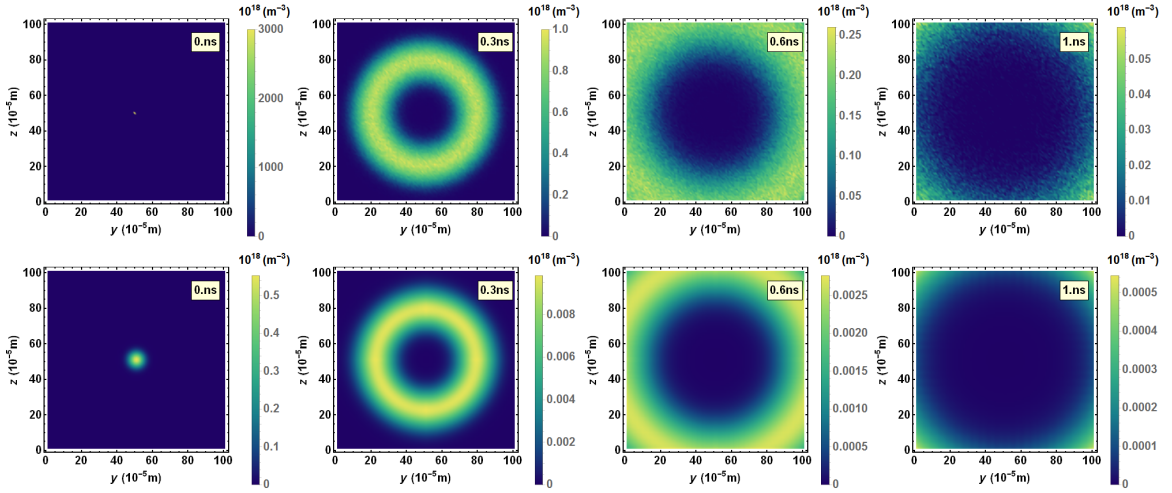


Figure 7: Snapshots of the particles densities in the yoz plane. The first and second rows correspond to the results given by JefiPIC and RBG-Maxwell. In JefiPIC the particles are initially located in the center grid as depicted by Fig. 6, while in RBG-Maxwell we have chosen a particle distribution where most particles are located in the center grid. The two scenarios are in general equivalent if we neglect the diffusions at the first few time steps.

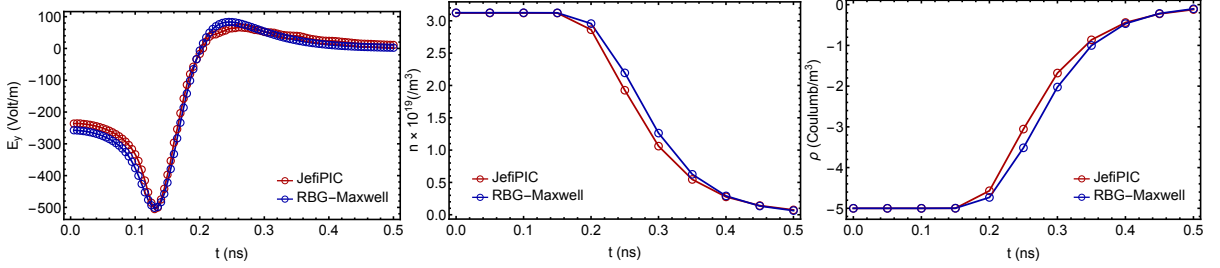


Figure 8: Comparisons of electric field E_y , total number density n and total charge density ρ . E_y is the measured electric field in the y direction at the observation point. n denote the total number of the particle densities, i.e., $n = \sum n_i$ where n_i is the number density in the i th grid. ρ is the total number of charge densities and $\rho = Qn$, where Q is the electric charge of an electron.

codes are generally in alignment. To further compare the outcomes of the two packages, we also present the measured electric field at the observation point, the total number densities, and total charge densities in Fig. 8. The results indicate a perfect correlation between the two packages.

2. Test of the collision term

We set the parameters $\hbar = c = \epsilon_0 = 1$ and $\lambda = 1.6 \times 10^{28}$ in NU. Two particle species a and b with the same mass 0.3 are chosen. For a box calculation, we restrict the particles in a spatial box of size $x_{\text{range}} \times y_{\text{range}} \times z_{\text{range}} = [-\frac{6}{0.197}, \frac{6}{0.197}] \times [-\frac{6}{0.197}, \frac{6}{0.197}] \times [-\frac{6}{0.197}, \frac{6}{0.197}]$ with grid size $n_x \times n_y \times n_z = 1 \times 1 \times 1$. The distribution functions f_a and f_b are confined in a six dimensional phase space of grid size $n_x \times n_y \times n_z \times n_{p_x} \times n_{p_y} \times n_{p_z} = 1 \times 1 \times 1 \times 35 \times 35 \times 35$. The momentum ranges are $p_{x,\text{range}} \times p_{y,\text{range}} \times p_{z,\text{range}} = [-2, 2] \times [-2, 2] \times [-2, 2]$. Here, species a and b are both classical particles, so we expect that the particles will obey the Boltzmann distribution at thermal equilibrium (for readers interested in the thermalization of Bosons and Fermions in BRG-Maxwell, please refer to Ref. [57]).

To see this, we choose the initial distribution function that is far from thermal equilibrium

$$f = f_0 \theta(|\mathbf{p}| - Q_s), \quad (46)$$

where the θ function is defined as

$$\theta(|\mathbf{p}| - Q_s) = \begin{cases} f_0 & \text{if } |\mathbf{p}| > Q_s \\ 0 & \text{else} \end{cases}. \quad (47)$$

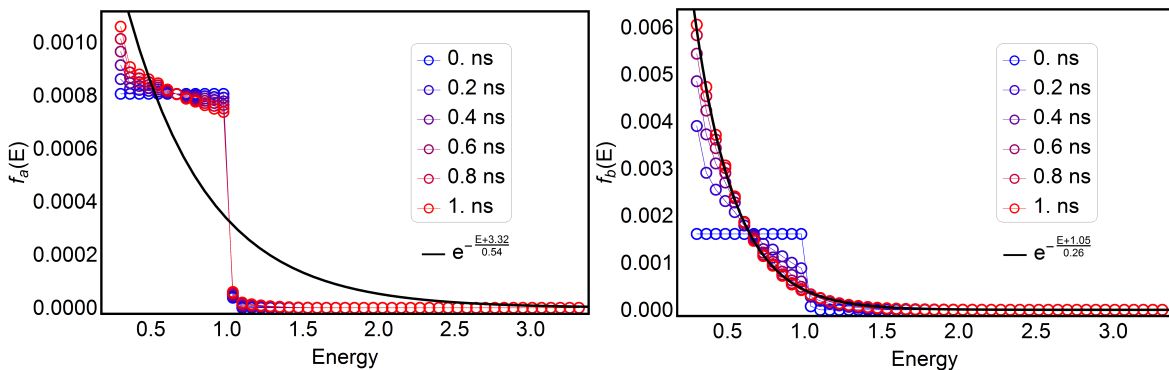


Figure 9: Time snapshots of the distribution functions for particle species a and b . The fitted thermal distributions are presented in the solid lines.

Table II: Performance of the RBG-Maxwell framework on 8 GPU cards. The memory occupancy is an average of all cards, and the evaluation time is measured for 10 time steps. Each GPU card has the maximum of 40 GB memory.

n_x, n_y, n_z	$n_{p_x}, n_{p_y}, n_{p_z}$	Memory occupancy (MB)	Evlaution time (hour)
21,21,21	11,11,11	18932	0.2
21,21,21	15,15,15	21313	0.43
31,31,31	11,11,11	26766	0.65
21,21,21	21,21,21	Out of memory	-

We set $Q_s = 1$, $f_{0,a} = 0.2$ and $f_{0,b} = 0.4$ in the calculation.

There are three types of collisions considered, i.e., $a+a \rightarrow a+a$, $b+b \rightarrow b+b$ and $a+b \rightarrow a+b$. The corresponding differential cross sections (see definition in Eq. (22)) take the following values

$$\begin{aligned}
 \frac{d\sigma}{d\Omega}|_{a+a \rightarrow a+a} &= 1, \\
 \frac{d\sigma}{d\Omega}|_{b+b \rightarrow b+b} &= 20, \\
 \frac{d\sigma}{d\Omega}|_{a+b \rightarrow a+b} &= 0.01.
 \end{aligned} \tag{48}$$

In the evolution, we use time step $dt = 0.0002/0.197$ and total number of time steps $n_{\text{total}} = 25000$. The configuration poses a strong collisional interaction for particle species b .

In Fig. 9, we depict the snapshots of the particle distributions. We can see that the distribution function of species b gradually achieves the Boltzmann distribution, while species a is still away from the thermal state. The calculation takes 0.32 hours on 1 Tesla A 100 card.

3. Performance on multi-GPUs

We assess the performance of the RBG-Maxwell on multi-GPUs in a more practical scenario, specifically, the quark-gluon plasma, which is the original context of the framework. In the simulation of quark-gluon matter, there are seven particle species interacting with each other, namely: u , d , and s quarks, their anti-quarks, and gluons. The potential collision types and the corresponding matrix elements can be found in Appendix VII. This intricate collisional quark-gluon plasma system which can be seamlessly extended to other plasma systems. Here, we use 8 NVIDIA A 100 cards in total. The spatial domain is divided into 8 sub-domains (Fig. 10). Adjacent sub-domains share two layers as the exchanging boundaries. For convenience, the number of grid sizes for all sub-domains are set to be the same. In Tab. II we conclude the memory consumption and the evaluation time for 10 time steps along with different grid numbers. From Tab. II it can be seen that the maximum number of total phase space grids on 8 GPU cards is about $\sim 31^3 \times 11^3 \approx 4 \times 10^7$. In real practice, we recommend the use of grid size $n_x, n_y, n_z, n_{p_x}, n_{p_y}, n_{p_z} = 21, 21, 21, 11, 11, 11$. Under this configuration, the total evaluation time of 10000 steps is about a week, which is acceptable in most heavy load computations.

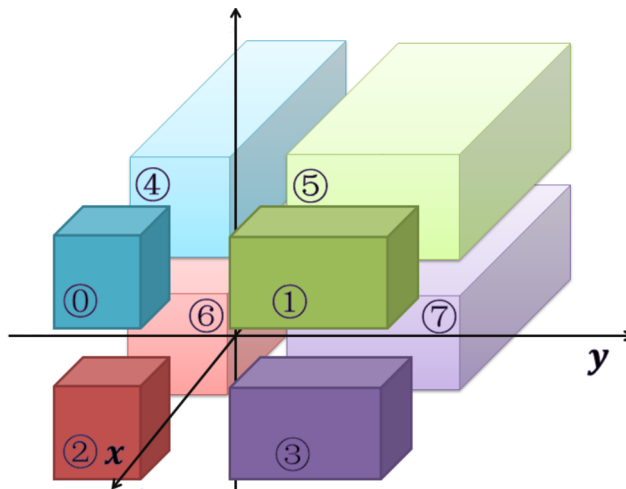


Figure 10: Division of the spatial domains. The numbers in the circles denote the indices of the sub-domains.

VI. CONCLUSION

In this study, we have detailed the RBG-Maxwell framework, a first-principle based relativistic collisional plasma simulator, designed for large-scale GPU clusters. We have outlined the essential equations, numerical algorithms, implementation details, and key testing outcomes of the framework. For those interested in utilizing this framework for practical problem-solving, please visit our introductory webpage: [<https://Juenjie.github.io> or <https://sunminmgyan.github.io>].

However, our work is not without its limitations. The current version of the RBG-Maxwell framework is resource-intensive, typically requiring eight GPU cards for practical applications. Despite our use of the Natural Unit to convert all physical quantities into the numerical range of GPU precision, certain plasma systems still necessitate careful calibration of the physical quantities. For instance, near space plasma conditions can present significant variations in velocities, masses, charges, spatial coordinates, and cross-sections. Additionally, our current framework struggles to cope with plasma systems that involve complex interactions with liquid and solid materials (such as the creation of an electromagnetic pulse, or the interaction of electromagnetic fields with the walls of the microwave tube). We intend to overcome these challenges in our future work, and plan to integrate cutting-edge deep learning techniques to boost the overall performance of the framework.

VII. ACKNOWLEDGMENTS

We extend our gratitude to Xin-Li Sheng from Central China Normal University for valuable discussions on the formalism, and to Shi Pu from the University of Science and Technology of China for insights on the physical implications of our work. This research has been funded by the National Science Foundation of China under grant number 12105227.

Appendix

Integration involving the Dirac delta

Dirac delta function is a generalized function which can be loosely thought of as a function on the real line which is zero everywhere except at the origin, where it is infinite,

$$\delta(x) = \begin{cases} +\infty, & x = 0 \\ 0, & x \neq 0 \end{cases}. \quad (49)$$

Delta function has the translation property

$$\int_{-\infty}^{\infty} f(x)\delta(x-X)dx = f(X), \quad (50)$$

from which we can work out the delta function corresponding to the momentum integration,

$$\begin{aligned} & \int d^3\mathbf{k}_2\delta^{(3)}(\mathbf{k}_1 + \mathbf{k}_2 - \mathbf{k}_3 - \mathbf{p})g(\mathbf{k}_2) \\ &= g(\mathbf{k}_3 + \mathbf{p} - \mathbf{k}_1)|_{\mathbf{k}_1+\mathbf{k}_2-\mathbf{k}_3-\mathbf{p}=0}, \end{aligned} \quad (51)$$

where $g(\mathbf{k}_2)$ represents an arbitrary function with variable \mathbf{k}_2 .

For composite delta function $\delta(g(x))$, if g has a real root x_0 , i.e., $g(x_0) = 0$, then

$$\delta(g(x)) = \frac{\delta(x-x_0)}{|g'(x_0)|}, \quad (52)$$

where we require the denominator $|g'(x_0)| \neq 0$. For continuously differentiable function $g(x)$, if it has more than one roots, the composition $\delta(g(x))$ is

$$\delta(g(x)) = \sum_i \frac{\delta(x-x_i)}{|g'(x_i)|}, \quad (53)$$

where the sum extends over all different roots.

Now we can work out the momentum integration involving $\delta^{(4)}(k_1 + k_2 - k_3 - p)$. From Eq. (51) we obtain

$$\begin{aligned} & \int \prod_{i=1}^3 d^3\mathbf{k}_i \delta^{(4)}(k_1 + k_2 - k_3 - p) \\ &= \int \prod_{i=1}^3 d^3\mathbf{k}_i \delta^{(3)}(\mathbf{k}_1 + \mathbf{k}_2 - \mathbf{k}_3 - \mathbf{p}) \\ & \quad \times \delta(k_1^0 + k_2^0 - k_3^0 - p^0) \\ &= \int d^3\mathbf{k}_1 d^3\mathbf{k}_3 \\ & \quad \times \delta(k_1^0 + k_2^0 - k_3^0 - p^0)|_{\mathbf{k}_2=\mathbf{k}_3+\mathbf{p}-\mathbf{k}_1}. \end{aligned} \quad (54)$$

Since the function

$$\begin{aligned} g(k_1^z) &\equiv k_1^0 + k_2^0|_{\mathbf{k}_2=\mathbf{k}_3+\mathbf{p}-\mathbf{k}_1} - k_3^0 - p^0 \\ &= \sqrt{(k_1^x)^2 + (k_1^y)^2 + (k_1^z)^2 + m^2c^2} \\ & \quad + k_2^0|_{\mathbf{k}_2=\mathbf{k}_3+\mathbf{p}-\mathbf{k}_1} - k_3^0 - p^0 \end{aligned} \quad (56)$$

has two roots

$$k_{1z}^{\pm} = \text{Root}[k_1^0 + k_2^0|_{\mathbf{k}_2=\mathbf{k}_3+\mathbf{p}-\mathbf{k}_1} - k_3^0 - p^0 = 0], \quad (57)$$

from the composition rule in Eq. (53), we have

$$\begin{aligned} & \delta(k_1^0 + k_2^0|_{\mathbf{k}_2=\mathbf{k}_3+\mathbf{p}-\mathbf{k}_1} - k_3^0 - p^0) \\ &= \sum_{i=\pm} \frac{1}{|J(k_{1z}^i)|} \delta(k_{1z} - k_{1z}^i), \end{aligned} \quad (58)$$

where the Jacobian function

$$\begin{aligned} J(k_{1z}^{\pm}) &= \frac{\partial g(k_1^z)}{\partial k_1^z}|_{k_1^z=k_{1z}^{\pm}} \\ &= \frac{k_{1z}^{\pm}}{(k_1^0)^{\pm}} - \frac{-k_{1z}^{\pm} + k_{3z} + p_z}{(k_2^0)^{\pm}}. \end{aligned} \quad (59)$$

In the above equation,

$$\begin{aligned} (k_1^0)^\pm &= \sqrt{(k_1^x)^2 + (k_1^y)^2 + (k_{1z}^\pm)^2 + m_1^2 c^2}, \\ (k_2^0)^\pm &= \sqrt{(\mathbf{k}_3 + \mathbf{p} - \mathbf{k}_1)^2 + m_2^2 c^2} \Big|_{k_{1z}^\pm = k_{1z}^\pm}, \end{aligned} \quad (60)$$

where $k_{1z}^\pm \equiv \frac{A \pm \sqrt{H}}{B}$, with A, B, H being the functions of $k_1^x, k_1^y, k_3^x, k_3^y, k_3^z, p_x, p_y, p_z, m_1, m_2, k_3^0$, and p^0 (see subsec. VII for details).

Substituting Eq. (58) into Eq. (55), and integrating out k_{1z} using the translation rule Eq. (50), we have

$$\begin{aligned} & \int \prod_{i=1}^3 d^3 \mathbf{k}_i \delta^{(4)}(k_1 + k_2 - k_3 - p) \\ &= \int d^3 \mathbf{k}_1 d^3 \mathbf{k}_3 \delta(k_1^0 + k_2^0 - k_3^0 - p^0) \\ &= \int d^3 \mathbf{k}_3 d k_1^x d k_1^y \sum_{i=\pm} \frac{1}{|J(k_{1z}^i)|}, \end{aligned} \quad (61)$$

which is the expression of Eq. (35).

Finding the expression of k_{1z}^\pm

The expression of k_{1z}^\pm can be found via Eq. (57). In the implementation, we write all components of the momenta explicitly, hence Eq. (57) becomes

$$\begin{aligned} k_{1z}^\pm &= \text{Root}[k_1^0 + k_2^0 \Big|_{\mathbf{k}_2 = \mathbf{k}_3 + \mathbf{p} - \mathbf{k}_1} - k_3^0 - p^0 = 0], \\ &= \text{Root} \left[\sqrt{(k_1^x)^2 + (k_1^y)^2 + (k_{1z}^\pm)^2 + m_1^2 c^2} - k_3^0 - p^0 \right. \\ &\quad \left. + \sqrt{(k_3^x + p_x - k_1^x)^2 + (k_3^y + p_y - k_1^y)^2 + (k_3^z + p_z - k_1^z)^2 + m_2^2 c^2} \right] \\ &= \frac{C1 \pm \sqrt{H}}{C2}, \end{aligned} \quad (62)$$

where

$$\begin{aligned}
C1 &= -(k_3^z + p_z) \\
&\times [c^2(-m_1^2 + m_2^2) - (k_3^0 + p^0)^2 - 2k_1^x(k_3^x + p_x) + (k_3^x + p_x)^2 \\
&\quad - 2k_1^y(k_3^y + p_y) + (k_3^y + p_y)^2 + (k_3^z + p_z)^2] \\
C2 &= 2(k_3^0 - k_3^z + p^0 - p_z)(k_3^0 + k_3^z + p^0 + p_z) \\
H &= (k_3^0 + p^0)^2 \\
&\times [(k_3^0)^4 - 2(k_3^0)^2(k_3^x)^2 + k_3^0 x^4 - 2(k_3^0)^2(k_3^y)^2 + 2(k_3^x)^2(k_3^y)^2 + (k_3^y)^4 - 2(k_3^0)^2(k_3^z)^2 \\
&\quad + 2(k_3^x)^2(k_3^z)^2 + 2(k_3^y)^2(k_3^z)^2 + (k_3^z)^4 - 2c^2(k_3^0)^2 m_1^2 - 2c^2(k_3^x)^2 m_1^2 - 2c^2(k_3^y)^2 m_1^2 + 2c^2(k_3^z)^2 m_1^2 \\
&\quad + c^4 m_1^4 - 2c^2(k_3^0)^2 m_2^2 + 2c^2(k_3^x)^2 m_2^2 + 2c^2(k_3^y)^2 m_2^2 + 2c^2(k_3^z)^2 m_2^2 - 2c^4 m_1^2 m_2^2 + c^4 m_2^4 \\
&\quad + 4(k_3^0)^3 p^0 - 4k_3^0(k_3^x)^2 p^0 - 4k_3^0(k_3^y)^2 p^0 - 4k_3^0(k_3^z)^2 p^0 - 4c^2 k_3^0 m_1^2 p^0 - 4c^2 k_3^0 m_2^2 p^0 \\
&\quad + 6(k_3^0)^2 (p^0)^2 - 2(k_3^x)^2 (p^0)^2 - 2(k_3^y)^2 (p^0)^2 - 2(k_3^z)^2 (p^0)^2 - 2c^2 m_1^2 (p^0)^2 - 2c^2 m_2^2 (p^0)^2 + 4k_3^0 (p^0)^3 + (p^0)^4 \\
&\quad - 4(k_3^0)^2 k_3^x p_x + 4k_3^0 x^3 p_x + 4k_3^x(k_3^y)^2 p_x + 4k_3^x(k_3^z)^2 p_x - 4c^2 k_3^x m_1^2 p_x + 4c^2 k_3^x m_2^2 p_x \\
&\quad - 8k_3^0 k_3^x p^0 p_x - 4k_3^x (p^0)^2 p_x - 2(k_3^0)^2 p_x^2 + 6(k_3^x)^2 p_x^2 + 2(k_3^y)^2 p_x^2 + 2(k_3^z)^2 p_x^2 \\
&\quad - 2c^2 m_1^2 p_x^2 + 2c^2 m_2^2 p_x^2 - 4k_3^0 p^0 p_x^2 - 2(p^0)^2 p_x^2 + 4k_3^x p_x^3 + p_x^4 - 4(k_3^0)^2 k_3^y p_y \\
&\quad + 4(k_3^x)^2 k_3^y p_y + 4(k_3^y)^3 p_y + 4k_3^y(k_3^z)^2 p_y - 4c^2 k_3^y m_1^2 p_y + 4c^2 k_3^y m_2^2 p_y - 8k_3^0 k_3^y p^0 p_y \\
&\quad - 4k_3^y (p^0)^2 p_y + 8k_3^x k_3^y p_x p_y + 4k_3^y p_x^2 p_y - 2(k_3^0)^2 p_y^2 + 2(k_3^x)^2 p_y^2 + 6k_3^y p_y^2 \\
&\quad + 2(k_3^z)^2 p_y^2 - 2c^2 m_1^2 p_y^2 + 2c^2 m_2^2 p_y^2 - 4k_3^0 p^0 p_y^2 - 2p^0 p_y^2 + 4k_3^x p_x p_y^2 + 2p_x^2 p_y^2 \\
&\quad + 4k_3^y p_y^3 + p_y^4 + 4k_3^z ((k_3^z)^2 + c^2(m_1^2 + m_2^2) - (k_3^0 + p^0)^2 + (k_3^x + p_x)^2 + (k_3^y + p_y)^2) p_z \\
&\quad + 2(3(k_3^z)^2 + c^2(m_1^2 + m_2^2) - (k_3^0 + p^0)^2 + (k_3^x + p_x)^2 + (k_3^y + p_y)^2) p_z^2 \\
&\quad + 4k_3^z p_z^3 + p_z^4 + 4(k_1^x)^2 (- (k_3^0 + p^0)^2 + (k_3^x + p_x)^2 + (k_3^z + p_z)^2) \\
&\quad + 4(k_1^y)^2 (- (k_3^0 + p^0)^2 + (k_3^y + p_y)^2 + (k_3^z + p_z)^2) - 4k_1^y (k_3^y + p_y) \\
&\quad \times (c^2(-m_1^2 + m_2^2) - (k_3^0 + p^0)^2 + (k_3^x + p_x)^2 + (k_3^y + p_y)^2 + (k_3^z + p_z)^2) - 4k_1^x (k_3^x + p_x) \\
&\quad \times (c^2(-m_1^2 + m_2^2) - (k_3^0 + p^0)^2 + (k_3^x + p_x)^2 - 2k_1^y (k_3^y + p_y) + (k_3^y + p_y)^2 + (k_3^z + p_z)^2)].
\end{aligned}$$

Therefore, k_{1z}^\pm are functions of $k_1^x, k_1^y, k_3^x, k_3^y, k_3^z, p_x, p_y, p_z, m_1, m_2, k_3^0$, and p^0 .

Relation between cross section and matrix element

For $2 \leftrightarrow 2$ process, we perform the integration of the differential probability per unit time,

$$\begin{aligned}
&\int d\omega \\
&= \int c(2\pi\hbar)^4 \delta^{(4)}\left(\sum_i p_i - \sum_j p_j\right) |M|^2 V \left[\prod_a \frac{\hbar c}{2E_a V} \right] \left[\prod_b \frac{d^3 \mathbf{k}_b}{(2\pi\hbar)^3} \frac{\hbar c}{2E_b} \right] \\
&= \int \delta^{(4)}\left(\sum_i p_i - \sum_j p_j\right) \frac{\hbar^2 c |M|^2}{V 64\pi^2 k_1^0 k_2^0 k_3^0 p^0} d^3 \mathbf{k}_3 d^3 \mathbf{p}.
\end{aligned} \tag{63}$$

Then we integrate out $d^3 \mathbf{k}_3$ using the delta function $\delta^{(3)}(\mathbf{p}_i - \mathbf{p}_j)$

$$\begin{aligned}
&\int d\omega \\
&= \int \delta(k_1^0 + k_2^0 - k_3^0 - \sqrt{|\mathbf{p}|^2 + m_p^2 c^2}) \frac{\hbar^2 c |M|^2}{V 64\pi^2 k_1^0 k_2^0 k_3^0 p^0} |\mathbf{p}|^2 d|\mathbf{p}| d\Omega.
\end{aligned} \tag{64}$$

Using the identity

$$\delta(k_1^0 + k_2^0 - k_3^0 - \sqrt{|\mathbf{p}|^2 + m_p^2 c^2}) = \frac{p^0}{|\mathbf{p}|} \delta(|\mathbf{p}| - \sqrt{(k_1^0 + k_2^0 - k_3^0)^2 - m_p^2 c^2})$$

we have

$$\begin{aligned}
& \int d\omega \\
&= \int \frac{p^0}{|\mathbf{p}|} \delta(|\mathbf{p}| - \sqrt{(k_1^0 + k_2^0 - k_3^0)^2 - m_p^2 c^2}) \frac{\hbar^2 c |M|^2}{V 64 \pi^2 k_1^0 k_2^0 k_3^0 p^0} |\mathbf{p}|^2 d|\mathbf{p}| d\Omega \\
&= \int \frac{\hbar^2 c |M|^2}{V 64 \pi^2 k_1^0 k_2^0 k_3^0 p^0} |\mathbf{p}| p^0 d\Omega \\
&\equiv \int \frac{c I}{k_1^0 k_2^0 V} d\sigma.
\end{aligned} \tag{65}$$

Therefore, we can obtain the relation between the cross section $d\sigma/d\Omega$ and matrix element M comparing the last two lines of Eq. (65),

$$\frac{d\sigma}{d\Omega} = \frac{\hbar^2 |M|^2 |\mathbf{p}|}{64 \pi^2 k_3^0 I}. \tag{66}$$

Matrix elements used in the model calculation

Table III: Matrix elements squared for all $2 \rightarrow 2$ parton scattering processes in QCD. The helicities and colors of all initial and final state particles are summed over. q_1 (\bar{q}_1) and q_2 (\bar{q}_2) represent quarks (antiquarks) of different flavors, and g represents the gluon. d_F and d_A denote the dimensions of the fundamental and adjoint representations of $SU_c(N)$ gauge group while C_F and C_A are the corresponding quadratic Casimirs. In a $SU_c(3)$ theory with fundamental representation fermions, $d_F = C_A = 3$, $C_F = 4/3$, and $d_A = 8$. The infrared divergence is suppressed by introducing a regulator in the denominator[98–100].

$ab \rightarrow cd$	$ M_{a(k_1)b(k_2) \rightarrow c(k_3)d(p)} ^2$
$q_1 q_2 \rightarrow q_1 q_2$	$8g^4 \frac{d_F^2 C_F^2}{d_A} \left(\frac{s^2 + u^2}{(t - m_g^2)^2} \right)$
$\bar{q}_1 q_2 \rightarrow \bar{q}_1 q_2$	
$q_1 \bar{q}_2 \rightarrow q_1 \bar{q}_2$	
$\bar{q}_1 \bar{q}_2 \rightarrow \bar{q}_1 \bar{q}_2$	
$q_1 q_1 \rightarrow q_1 q_1$	$8g^4 \frac{d_F^2 C_F^2}{d_A} \left(\frac{s^2 + u^2}{(t - m_g^2)^2} + \frac{s^2 + t^2}{(u - m_g^2)^2} \right) + 16g^4 d_F C_F \left(C_F - \frac{C_A}{2} \right) \frac{s^2}{(t - m_g^2)(u - m_g^2)}$
$\bar{q}_1 \bar{q}_1 \rightarrow \bar{q}_1 \bar{q}_1$	
$q_1 \bar{q}_1 \rightarrow q_1 \bar{q}_1$	$8g^4 \frac{d_F^2 C_F^2}{d_A} \left(\frac{s^2 + u^2}{(t - m_g^2)^2} + \frac{u^2 + t^2}{s^2} \right) + 16g^4 d_F C_F \left(C_F - \frac{C_A}{2} \right) \frac{u^2}{(t - m_g^2)s}$
$q_1 \bar{q}_1 \rightarrow q_2 \bar{q}_2$	$8g^4 \frac{d_F^2 C_F^2}{d_A} \frac{t^2 + u^2}{s^2}$
$q_1 \bar{q}_1 \rightarrow gg$	$8g^4 d_F C_F^2 \left(\frac{u}{(t - m_g^2)} + \frac{t}{(u - m_g^2)} \right) - 8g^4 d_F C_F C_A \left(\frac{t^2 + u^2}{s^2} \right)$
$q_1 g \rightarrow q_1 g$	$-8g^4 d_F C_F^2 \left(\frac{u}{s} + \frac{s}{(u - m_g^2)} \right) + 8g^4 d_F C_F C_A \left(\frac{s^2 + u^2}{(t - m_g^2)^2} \right)$
$\bar{q}_1 g \rightarrow \bar{q}_1 g$	
$gg \rightarrow gg$	$16g^4 d_A C_A^2 \left(3 - \frac{su}{(t - m_g^2)^2} - \frac{st}{(u - m_g^2)^2} - \frac{tu}{s^2} \right)$

-
- [1] J. P. Verboncoeur, Plasma Physics and Controlled Fusion **47**, 231 (2005).
[2] K. Fukushima, Reports on Progress in Physics **80**, 022301 (2016).
[3] S. Lee, P. H. Yoon, E. Lee, and W. Tu, The Astrophysical Journal **924**, 36 (2022).
[4] G. Singh, A. K. Singh, and T. Nandi, The European Physical Journal D **76**, 62 (2022).

- [5] J. Li, H. Y. Guo, B. N. Wan, X. Z. Gong, Y. F. Liang, G. S. Xu, K. F. Gan, J. S. Hu, H. Q. Wang, L. Wang, et al., *Nature Physics* **9**, 817–821 (2013).
- [6] J. Li, Y. Wan, and the EAST team, *Engineering* **7**, 1523 (2021).
- [7] J. L. Gilbert, W. A. Radasky, and E. B. Savage, *IEEE Transactions on Electromagnetic Compatibility* **55**, 446 (2013).
- [8] J. Wang, L. Liu, S. Niu, Y. Zuo, Y. Gao, J. Zhu, X. Zhang, Y. Li, and X. Li, *Modern Applied Physics* **14**, 010101 (2023).
- [9] B. A. Wilson, A. Miloshevsky, D. A. Hooper, and N. A. Peters, *Physical Review Applied* **16**, 064049 (2021).
- [10] J. Wang, Z. Chen, Y. Wang, D. Zhang, C. Liu, Y. Li, H. Wang, H. Qiao, M. Fu, and Y. Yuan, *Physics of Plasmas* **17**, 073107 (2010).
- [11] J. Wang, G. Wang, D. Wang, S. Li, and P. Zeng, *Scientific Reports* **8**, 6978 (2018).
- [12] X. Li, J. Wang, J. Sun, Z. Song, H. Ye, Y. Zhang, L. Zhang, and L. Zhang, *IEEE Transactions on Electron Devices* **60**, 2931 (2013).
- [13] D. F. Higgins, K. S. H. Lee, and L. Marin, *IEEE Transactions on Electromagnetic Compatibility EMC-20*, 14 (1978).
- [14] J. Chen, J. Wang, Z. Chen, and Z. Ren, *IEEE Transactions on Nuclear Science* **67**, 818 (2020).
- [15] J. Chen, J. Wang, Z. Chen, Z. Ren, and H. Qiao, *IEEE Transactions on Electromagnetic Compatibility* **64**, 1182 (2022).
- [16] R. A. Treumann, *The Astronomy and Astrophysics Review* **17**, 409–535 (2009).
- [17] C. Shen, Z. Qiu, H. Song, J. Bernhard, S. Bass, and U. Heinz, *Computer Physics Communications* **199**, 61 (2016).
- [18] R. Kissmann, J. Kleimann, B. Krebl, and T. Wiengarten, *The Astrophysical Journal Supplement Series* **236**, 53 (2018).
- [19] U. Ziegler, *Computer Physics Communication* **116**, 65 (1999).
- [20] D. W. Hewett, S. H. Brecht, and D. J. Larson, *Journal of Geophysical Research* **116**, A11310 (2011).
- [21] G. Peng, J. Zhang, J. Chen, T. Du, and H. Xie, *Physics of Fluids* **33**, 076602 (2021).
- [22] D. Groseelj, A. Mallet, N. F. Loureiro, and F. Jenko, *Physical Review Letters* **120**, 105101 (2018).
- [23] D. Groseelj, C. H. Chen, A. Mallet, R. Samtaney, K. Schneider, and F. Jenko, *Physical Review X* **9**, 031037 (2019).
- [24] Z. Xu, K. Zhou, P. Zhuang, and C. Greiner, *Physical Review Letters* **114**, 18 (2015).
- [25] M. Greif, C. Greiner, and Z. Xu, *Physical Review C* **96**, 014903 (2017).
- [26] K. M., *Journal of Physics D: Applied Physics* **42**, 194013 (2009).
- [27] J. Dijk, van, K. Peerenboom, M. Jimenezdiaz, D. Mihailova, and J. Mullen, van der, *Journal of Physics D: Applied Physics* **42**, 194012 (2009), ISSN 0022-3727.
- [28] R. Bird, N. Tan, S. V. Luedtke, S. L. Harrell, M. Taufer, and B. Albright, *IEEE Transactions on Parallel and Distributed Systems* **33**, 952 (2022).
- [29] M. Klich, J. Lower, S. Wilczek, T. Mussenbrock, and R. P. Brinkmann, *Plasma Sources Science and Technology* **31**, 27 (2022).
- [30] T. D. Arber, K. Bennett, C. S. Brady, A. Lawrence-douglas, M. G. Ramsay, N. J. Sircombe, P. Gillies, R. G. Evans, H. Schmitz, A. R. Bell, et al., *Plasma Physics and Controlled Fusion* **57**, 113001 (2015).
- [31] J. Wang, D. Zhang, C. Liu, Y. Li, Y. Wang, H. Wang, H. Qiao, and X. Li, *Physics of Plasmas* **16**, 033108 (2009).
- [32] J. M. Dawson, *Review of Modern Physics* **55**, 403 (1983).
- [33] J. Chen and J. Zhang, *Nuclear Engineering and Technology* **54**, 3415 (2022), ISSN 1738-5733, URL <https://www.sciencedirect.com/science/article/pii/S173857332200239X>.
- [34] I. Grishmanovskii, T. Song, O. Soloveva, C. Greiner, and E. Bratkovskaya, *Physical Review C* **106**, 014903 (2022).
- [35] N. Rostoker, *Physics of Fluids* **7**, 1217 (1964).
- [36] T. W. Tuer and G. S. Springer, *Computers and Fluids* **1**, 399 (1973).
- [37] Y. Li and X. Huang, *Physical Review D* **107**, 094028 (2023).
- [38] J. Zhang, X. Sheng, S. Pu, J. Chen, G. Peng, and Q. Wang, *Physical Review Research* **4**, 033138 (2022).
- [39] D. Pan, C. Zhong, C. Zhuo, and W. Tan, *Applied Sciences* **8**, 746 (2018).
- [40] R. Holland, *IEEE Transactions on Electromagnetic Compatibility* **37**, 433 (1995).
- [41] G. Dimarco and L. Pareschi, *Acta Numerica* **23**, 369 (2014).
- [42] P. Romatschke, M. Mendoza, and S. Succi, *Physical Review C* **84**, 034903 (2011).
- [43] W. Verdiera, P. Kestenerb, and A. Cartalade, *Computer Methods in Applied Mechanics and Engineering* **370**, 113266 (2020).
- [44] M. Januszewski and M. Kostur, *Computer Physics Communications* **185**, 2350 (2014).
- [45] F. Pelusi, M. Lulli, M. Sbragaglia, and M. Bernaschi, *Computer Physics Communications* **273**, 108259 (2022).
- [46] X. Zhang, X. Chen, M. M. Islam, H. Yu, J. Gomezpaz, Y. Andreopoulos, J. M. McDonough, and L. Zhu, *Scientific reports* p. 1697 (2022).
- [47] S. J. J. Hu and A. Alexeenko, in *31st International Symposium on Rarefied Gas Dynamics: RGD31* ((AIP Publishing, 2019).
- [48] H. Wu, J. Zhang, L. Pang, and Q. Wang, *Computer Physics Communications* **248**, 106962 (2019).
- [49] J. Zhang and H. Wu, *Computer Physics Communications* **251**, 107240 (2020).
- [50] M. Peskin, *An Introduction To Quantum Field Theory, Student Economy Edition* (CRC Press, 2018).
- [51] M. E. Peskin and D. V. Schroeder, *An introduction to quantum field theory* (CRC Press, Boca Raton, FL, 2018), ISBN 9780813350196.
- [52] J. Zhang, J. Chen, G. Peng, T. Du, and H. Xie, *Computer Physics Communications* **276**, 108328 (2022).
- [53] A. Kurkela and A. Mazeliauskas, *Physical Review Letters* **122**, 142301 (2019).
- [54] L. Keegan, A. Kurkela, A. Mazeliauskas, and D. Teaney, *Journal of High Energy Physics* **08**, 171 (2018).
- [55] A. Kurkela and A. Mazeliauskas, *Physical Review D* **99**, 054018 (2019).
- [56] A. Kurkela, A. Mazeliauskas, J. Paquet, S. Schlichting, and D. Teaney, *Physical Review C* **99**, 034910 (2019).

- [57] J. Zhang, H. Wu, S. Pu, G. Qin, and Q. Wang, *Physical Review D* **102**, 074011 (2020).
- [58] S. Imada, *The Astrophysical Journal Letters* **914**, L28 (2021).
- [59] T. M. Mishonov, I. M. Dimitrova, and A. M. Varonov, *The Astrophysical Journal* **916**, 18 (2021).
- [60] J. Ren, Z. Deng, W. Qi, B. Chen, B. Ma, X. Wang, S. Yin, J. Feng, W. Liu, Z. Xu, et al., *Nature Communications* p. 5157 (2020).
- [61] B. Ma, J. Ren, S. Wang, D. H. H. Hoffmann, Z. Deng, W. Qi, X. Wang, S. Yin, J. Feng, Q. Fan, et al., *The Astrophysical Journal* **920**, 106 (2021).
- [62] Y. Zhao, Y. Zhang, R. Cheng, B. He, C. Liu, X. M. Zhou, Y. Lei, Y. Y. Wang, J. R. Ren, X. Wang, et al., *Physical Review Letters* **126**, 115001 (2021).
- [63] R. Pasechnik and M. Sumera, *Universe* **3**, 61 (2017).
- [64] W. Greiner, S. Schramm, and E. Stein, *Quantum Chromodynamics* (Springer Berlin Heidelberg, 2007).
- [65] S. Weinberg, *The Quantum Theory of Fields* (Cambridge University Press, 1995).
- [66] A. H. Kritz and G. Sandri, *Physics Today* **19**, 57 (1966).
- [67] P. Ehrenfest, *The concept foundations of the statistical approach in mechanics* (Dover Publications, 1959), ISBN 0486662500.
- [68] F. M. Ramos, R. R. Rosa, and L. A. Bambace, *Physical Review Letters* **86**, 2938 (2001).
- [69] L. Boltzmann, *History of Modern Physical Sciences* **1**, 262 (2003).
- [70] O. Jefimenko, *Electricity and magnetism : an introduction to the theory of electric and magnetic fields* (Electret Scientific Co, Star City, W. Va, 1989), ISBN 9780917406089.
- [71] M. Mason, *Physical Review* **15**, 312 (1920).
- [72] X. Shao, *Journal of Geophysical Research: Atmospheres* **121**, 3363 (2016).
- [73] K. Yee, *IEEE Transactions on Antennas and Propagation* **14**, 302 (1966).
- [74] W. F. Hall and A. V. Kabakian, *Journal of Computational Physics* **194**, 140 (2004).
- [75] T. S. ANGELL and A. KIRSCH, *SIAM Journal on Applied Mathematics* **52**, 1597–1610 (1992).
- [76] J. H. ADLER, X. HU, and L. T. ZIKATANOV, *SIAM Journal on Applied Mathematics* **39**, S3 (2017).
- [77] J. Brackbill, *Journal of Computational Physics* **227**, 6715 (2008).
- [78] S. Shuangyuan, *Physical Review* **172**, 1310 (1968).
- [79] J. C. Piquette, *Physics Today* **65**, 10 (2012).
- [80] R. Okuta, Y. Umno, D. Nishino, S. Hido, and C. Loomis, in *Proceedings of Workshop on Machine Learning Systems (LearningSys) in The Thirty-first Annual Conference on Neural Information Processing Systems (NIPS)* (2017), URL http://learningsys.org/nips17/assets/paper/paper_16.pdf.
- [81] *Cupy*, <https://docs.cupy.dev/en/stable/index.html>.
- [82] S. K. Lam, A. Pitrou, and S. Seibert, in *Proceedings of the Second Workshop on the LLVM Compiler Infrastructure in HPC - LLVM* (ACM Press, 2015).
- [83] *Numba*, <https://numba.pydata.org>.
- [84] H. Nishikawa, *Journal of Computational Physics* **229**, 315 (2010).
- [85] F. Ali and D. F. Mayers, *Journal of Computational and Applied Mathematics* **58**, 201 (1995).
- [86] G. de Vahl Davis and G. D. Mallinson, *Computers and Fluids* **4**, 29 (1976).
- [87] B. M. Chencharpentier and H. V. Kojouharov, *Mathematical and Computer Modelling* **57**, 2177 (2013).
- [88] M. K. Gobbert, A. Meister, and S. Wallbaum, *Proceedings in Applied Mathematics and Mechanics* **14**, 965 (2014).
- [89] B. Parent, *Computers and Fluids* **44**, 238 (2011).
- [90] W. K. Anderson, J. L. Thomas, and B. V. Leer, *AIAA Journal* **24**, 1453 (1986).
- [91] S. Gottlieb and C. Shu, *Mathematics of Computation* **67**, 221 (1988).
- [92] G. LeBeau, *Computer Methods in Applied Mechanics and Engineering* **174**, 319 (1999).
- [93] S. K. Stefanov, *Physics of Fluids* **31**, 067104 (2019).
- [94] P. Moritz, R. Nishihara, S. Wang, R. L. A. Tumanov, E. Liang, M. Elibol, Z. Yang, W. Paul, I. Jordan, and I. Stoica, in *13th USENIX Symposium on Operating Systems Design and Implementation (OSDI 18)* (USENIX Association, Carlsbad, CA, 2018), pp. 561–577, ISBN 978-1-931971-47-8.
- [95] *Ray*, <https://ray.io>.
- [96] C. Lin, A. Ecer, J. Periaux, N. Satofuka, and P. Fox, eds., *Parallel computational fluid dynamics 1998: development and application of parallel technology* (North Holland, 1999), ISBN 978-0444828507.
- [97] D. Keyes, A. Ecer, J. Periaux, N. Satofuka, and P. Fox, eds., *Parallel computational fluid dynamics 1999: towards teraflops, optimization and novel formulations* (North Holland, 2000), ISBN 978-0444828514.
- [98] P. B. Arnold, G. D. Moore, and L. G. Yaffe, *Journal of High Energy Physics* **2003**, 030 (2003).
- [99] J. Chen, Y. Liu, Y. Song, and Q. Wang, *Physical Review D* **87**, 036002 (2013).
- [100] X. Zhang and W. Chao, *Nuclear Physics A* **628**, 161 (1998).
- [101] Z. Xu and C. Greiner, *The European Physical Journal C* **49**, 187 (2006).
- [102] Y. Wang, J. Wang, Z. Chen, G. Cheng, and P. Wang, *Computer Physics Communications* **205**, 1 (2016).
- [103] H. Spohn, *Loschmidt's reversibility argument and the H-theorem* (Springer, 1997), ISBN 978-1-4899-0268-9.
- [104] R. Courant, K. O. Friedrichs, and H. Lewy, *Mathematische Annalen* **100**, 32 (1928).
- [105] L. Pauling, *College Chemistry*, vol. 57 (W.H. Freeman edition, 1964).
- [106] N. Bezginov, T. Valdez, M. Horbatsch, A. Marsman, A. C. Vutha, and E. A. Hessels, *Science* **365**, 1007 (2019).
- [107] P. K. Mandal and E. Arunan, *Journal of Chemical Physics* **114**, 3880 (2001).
- [108] G. V. VERESHCHAGIN and A. G. AKSENOV, *Relativistic Kinetic Theory* (Cambridge University Press, 2017).

- [109] J. Chen, J. Wang, Y. Tao, Z. Chen, Y. Wang, and S. Niu, *IEEE Transactions on Nuclear Science* **66**, 820 (2019).
- [110] B. Mortier, P. Robbe, M. Baelmans, and G. Samaey, *Journal of Computational Physics* **450**, 110736 (2022).
- [111] J. Ouyang, Y. Ma, and F. Shao, *IEEE Transactions on Nuclear Science* **61**, 1433 (2014).
- [112] H. Xu, J. Ouyang, S. Wang, Y. Liu, and X. Sun, *Nuclear Science and Techniques* **30**, 1001 (2019).